An analytical cohesive crack modeling approach to the edge debonding failure of FRP-plated beams

An analytical cohesive crack modeling approach to the edge debonding failure of FRP-plated beams

Pietro Cornetti[1], Mauro Corrado[1], Laura De Lorenzis[2], Alberto Carpinteri[1]

[1]Department of Structural, Building and Geotechnical Engineering, Politecnico di Torino, Italy
E-mail: pietro.cornetti@polito.it, mauro.corrado@polito.it, alberto.carpinteri@polito.it

[2]Institut für Angewandte Mechanik, Technische Universität Braunschweig, Germany
E-mail: l.delorenzis@tu-braunschweig.de

Abstract. This paper focuses on the prediction of edge debonding for a beam retrofitted with a Fiber-Reinforced Polymer plate. This failure mechanism, also known as plate-end debonding, stems from the concentration of interfacial stresses arising at the termination of the strengthening plate. Early models of edge debonding adopted failure criteria based on interfacial stresses. However, due to the typically catastrophic nature of this failure mechanism, approaches based on Linear Elastic Fracture Mechanics (LEFM) became increasingly established. In this paper, the problem is addressed by means of the Cohesive Crack Model (CCM) and of the Finite Fracture Mechanics (FFM). These models are able to bridge the gap between the stress- and the energy-based approaches and nevertheless have been used in a limited number of analytical studies to date. Based on a cohesive interface law with linear softening, closed-form solutions are derived for the interfacial stresses and the load-displacement curves, as well as for the ultimate load. It is found that LEFM usually overestimates the debonding load, thus justifying the need for the proposed approach; on the other hand, debonding load estimates based on FFM are in excellent agreement with the CCM predictions. Finally, a parametric analysis highlights the effect of the geometry/material properties on the structural response, as well as the ductile-to-brittle transition and the possible occurrence of structural instabilities depending on the test controlling parameters.

1. Introduction

Among the strengthening techniques for civil engineering structures and in particular for concrete structures, bonding of Fibre-Reinforced Polymer (FRP) sheets is nowadays widely employed. The advantages of this technique are several. FRP laminates are easy to install and cause a minimal increase in size of the structure; furthermore, they possess high strength, light weight and excellent durability.

The structural behaviour of FRP-strengthened members is substantially different from that of the original un-strengthened members and, even more importantly, new failure modes may occur (Carpinteri et al., 2009a; De Lorenzis, 2012). Among the observed failure modes, the so-called edge debonding of the FRP plate (also known as plate-end debonding) deserves a special attention because of its catastrophic nature (Pellegrino & D'Antino, 2013). The present paper focuses on the analytical prediction of this failure mechanism.

Early predictive models of edge debonding failure were based on setting limits to the stresses at the FRP-substrate interface (Taljsten, 1997; Smith & Teng, 2001). However, because of the brittleness of the debonding process, an energy approach was later recognized as more appropriate, since stress-based failure criteria are more suitable for gradual and ductile failures. Within an analytical context, energy-based fracture criteria have been recently proposed by Rabinovitch (2004), Colombi (2006), Greco et al. (2007) and Carpinteri et al. (2009b) by applying the Linear Elastic Fracture Mechanics (LEFM) concept of strain energy release rate.

With the objective to bridge the gap between the stress- and energy-based approaches, in the present paper the problem is addressed by modelling the debonding crack at the FRP-substrate interface by a Cohesive Crack Model (CCM). While several investigations on the debonding process in FRP-concrete joints subjected to pure shear have adopted the CCM either in analytical (Yuan et al., 2004; Leung & Tung, 2006; Cottone & Giambanco, 2009; Carpinteri & Cornetti, 2011; Caggiano et al., 2012) or in numerical (Ferracuti et al., 2006; Dehghani et al., 2012) form, a more limited number of analytical studies have been conducted on cohesive crack modelling of interfacial stresses in plated beams since the papers by Rabinovitch (2008a, 2008b). While Carpinteri & Paggi (2010) focused on numerical methods, De Lorenzis & Zavarise (2009) and Bennati et al. (2012) presented the cohesive crack analytical solutions for edge debonding of a beam under three-point bending (TPB) and constant bending moment, respectively.

The present work focuses on edge debonding of an FRP strengthened beam under a TPB loading condition, extending previous results given in Carpinteri et al. (2009b) and De Lorenzis & Zavarise (2009). With respect to the paper by Carpinteri et al. (2009b), the condition of elastic-perfectly brittle interface has been relaxed - thus highlighting the effect of the interfacial softening - while the stress analysis carried out in De Lorenzis and Zavarise (2009) has been extended to understand how the geometry and material parameters affect the global structural response and, particularly, the ductile-to-brittle transition with the possible occurrence of structural instabilities.

Throughout the paper, linear-elastic behaviour for the adherent materials is assumed (all non-linearities are concentrated at the interface) and the peeling stresses at the interface are neglected. While being an oversimplification of the actual behaviour, these assumptions are suitable to highlight the essential features of the debonding process and the role played by the most significant variables. Furthermore they enable the development of a fully analytical solution for the stress fields and the structural response, which turns out to be affected only by four dimensionless parameters.

The plan of the paper is as follows. After this Introduction, the LEFM solution based on the assumption of planar cross section for the two-layer composite beam (Equivalent Beam model) is recalled to be used later for comparison purposes. In Section 3 the basic assumptions of the model are outlined and the second-order differential equation governing the interfacial shear stress field is derived. Section 4 is devoted to the interfacial cohesive law, here assumed to be bi-linear. In Section 5 the various stages of the debonding process are analyzed and explicit expressions for the shear stress and the relative sliding displacement at the interface are given. Section 6 deals with the structural response and provides the analytical expression for load, mid-span deflection and crack mouth sliding displacement during the debonding process. The possible occurrence of structural instabilities depending on the test control variable is highlighted. Section 7 provides the analytical details to compute the maximum load, along with a simplified expression; the predictions obtained through the CCM are further compared with those from the Finite Fracture Mechanics (FFM) criterion. Section 8 presents a parametric analysis showing how the structural behaviour is affected by the geometry/material properties characterizing the problem at hand. Finally Section 9 provides some conclusions.

2. Equivalent beam model and LEFM

Let us consider the plated beam in fig. 1, i.e. a beam with a rectangular cross section strengthened by an FRP strip at its bottom. In the following, the quantities with subscript “b” refer to the beam to be strengthened and the ones with subscript “r” to the FRP reinforcement. Thus E_b, E_r are the Young’s moduli of the beam and of the FRP reinforcement; h_b, h_r are their respective thicknesses; t_b and t_r their widths. The ratio of the axial stiffness of the FRP to the one of the beam is denoted by ρ:

$$\rho = \frac{E_r h_r t_r}{E_b h_b t_b} \tag{1}$$

and represents the mechanical percentage of reinforcement.

The beam span is $2l$ and P is the concentrated load acting at the beam mid-span. The length of the FRP strip (i.e. the initial bond length) is $2z_r$, while a is the distance between the FRP termination and the support. Because of structural symmetry we can analyze only half of the beam (see fig. 2a). Focusing on the right half and placing the origin of the axial coordinate z at the beam mid-span, the shear force is $T = -P/2$ and the bending moment is $M = P(l-z)/2$.

The easiest model for plated beams is the so-called Equivalent Beam (EB) model, based on the assumption of a planar cross section for the whole structure. It assumes a perfect bonding between the beam and the reinforcement, i.e. an infinitely stiff interface. Although in the following sections we will remove such an assumption, it is here useful to recall the main EB model outcomes for the sake of the later comparison.

The thickness of the FRP strip is usually two orders of magnitude smaller than the beam height (especially if concrete beams are considered). This implies that we can model the reinforcement as if it were concentrated at the beam soffit (fig. 2). Such an approximation yields two advantages. First, it greatly simplifies the resulting formulae without a significant decrease in precision. For instance, the moment of inertia is underestimated of less than 1% with respect to its exact value for a typical ratio of the Young moduli ($E_r/E_b = 7$) and an height ratio h_r/h_b smaller than 0.02 (note that an even better approximation is obtained by concentrating the reinforcement at its mid-plane while considering a fictitious beam height equal to $h_b + h_r/2$). Even more important, modelling the FRP as if it were concentrated on a line is coherent with the assumption of negligible bending stiffness of the reinforcement that will be adopted in the next section, so that the present EB-model solution turns out to be the asymptotic case (for an infinitely stiff and perfectly brittle interface) of the cohesive interface model developed in the remaining part of the paper.

Simple computations lead to the position d of the centre of gravity of the reinforced section (with respect to the bottom of the beam, see fig. 2b) and its moment of inertia (with respect to the x axis):

$$d = \frac{h_b}{2(1+\rho)} \tag{2}$$

$$I = \frac{1+4\rho}{1+\rho} I_b \tag{3}$$

where $I_b = t_b\, h_b^3 / 12$ is the moment of inertia of the plain beam section. The shear stress τ_{Jou} at the interface and the normal stress σ_r in the reinforcement are, according to Navier's and Jourawsky's formulae respectively:

$$\sigma_r = \frac{3\rho}{1+4\rho} \frac{P(l-z)}{t_r h_r h_b} \tag{4}$$

$$\tau_{Jou} = \frac{3\rho}{1+4\rho} \frac{P}{t_r h_b} \tag{5}$$

the latter value being given as absolute value. A first rough estimate of the load causing FRP edge debonding can be obtained assuming that the delamination occurs whenever the interfacial shear stress reaches the interfacial shear strength τ_p. The corresponding critical load P_{Jou} is thus equal to:

$$P_{Jou} = \frac{1+4\rho}{3\rho} \tau_p t_r h_b \tag{6}$$

which is independent of the reinforcement length.

The debonding load estimate (6) derives from a stress criterion. To obtain the estimate based on the energy criterion (i.e. LEFM) we have to evaluate the strain energy release rate $\mathcal{G}$. For load-controlled conditions, $\mathcal{G}$ is given by the derivative of the strain energy Φ with respect to the crack area A, i.e. by the difference in the strain energy of the differential beam element at the FRP edge with and without the reinforcement divided by the infinitesimal crack growth $t_r da$. Hence, according to the EB model, the strain energy release rate reads (Carpinteri et al., 2009b):

$$\mathcal{G} = \frac{\mathrm{d}\Phi}{\mathrm{d}A} = \frac{1}{t_r}\left[\frac{M^2}{2E_b I_b} - \frac{M^2}{2E_b I}\right]_{z=z_r} \tag{7}$$

By eqn (3), we get:

$$\mathcal{G} = \frac{9\rho}{2(1+4\rho)}\frac{P^2(l-z_r)^2}{t_r t_b h_b^3 E_b} \tag{8}$$

According to LEFM, debonding occurs whenever $\mathcal{G}$ reaches its critical value $\mathcal{G}_c$, i.e. the interfacial fracture energy. The corresponding debonding load P_{LEFM} is therefore:

$$P_{LEFM} = \frac{\sqrt{1+4\rho}}{3\rho}\frac{t_r h_b}{l-z_r}\sqrt{2\mathcal{G}_c E_r h_r} \tag{9}$$

Equation (9) represents the debonding load according to the LEFM-EB model. Differently from what predicted by the stress criterion (6), eqn (9) shows that the debonding process is unstable (under load control), since the load causing the FRP debonding strongly decreases as the bond length z_r decreases. This catastrophic behavior, typical of plated beams failing by edge debonding, explains the considerable attention of researchers to this failure mechanism.

Although LEFM-EB model is able to predict the basic features of the plate end debonding collapse, the more refined cohesive analysis provided in the remaining part of the paper shows that (for a given fracture energy) the failure load estimate (9) is generally an overestimate. This implies that an uncritical application of LEFM is potentially dangerous and not conservative.

As far as displacements are concerned, according to the EB model, the elementary beam theory provides the following value for the mid-span deflection v_{EB}:

$$v_{EB} = \frac{P(2l)^3}{48E_b I}\left[1 + \frac{3\rho}{1+\rho}\left(1-\frac{z_r}{l}\right)^3\right] \tag{10}$$

where the term outside the square bracket represents the mid-span deflection if the beam were reinforced over the whole span; or, equivalently, the second term inside the square bracket represents the relative increment of deformability due to a bond length z_r shorter than the beam length l.

For an ideal test where it is possible to control the advancement of the debonding crack (i.e. z_r), the load-displacement curve is simply given by eqns (9) and (10) (provided that eqn (9) is substituted into eqn (10)) while the bond length decreases from its initial value to zero. A typical plot is drawn in fig. 3, where the load and the displacement have been normalized by their respective values at the onset of debonding, so that the structural response depends only on two parameters: the mechanical reinforcement percentage ρ and the relative reinforcement length z_r / l.

After a linear elastic loading phase, debonding starts and it ends when the FRP plate is completely detached. Then the load can increase again, the loading curve being now represented by the straight line characterizing the linear elastic behaviour of the un-strengthened beam. Up to a multiplicative factor, the area between the thick curve and the dashed line represents the energy spent to separate the reinforcement from the beam. It is evident that a snap-through instability occurs if the test is load-controlled and that a snap-back instability takes place if the test is (mid-span) displacement-controlled.

3. Governing equation

The EB model presented in the previous section takes neither the interface compliance nor its softening behaviour into account. It is easily argued that, wishing to tackle the debonding process, a more realistic description of the FRP-substrate interface is needed. We achieve this goal by modelling the interface as a cohesive interface, the remaining structural components being considered as linear elastic. Since our goal is the development of an analytical model, we introduce the simplifying assumption of negligible bending stiffness of the reinforcement (with respect to the one of the beam), which, for the present geometry, is justified by the thinness of the FRP plate. Consequently the interface works as a shear lag, i.e. it transfers only tangential stresses from the beam to the FRP reinforcement, and peeling stresses are neglected. Although reasonable in the present case, the assumption of negligibility of the peeling stresses must be carefully considered because it may yield an overestimate of the failure load. In fact, peeling stresses make the delamination a mixed mode fracture process, which is usually characterized by a fracture energy lower than the one related to the pure sliding mode.

More refined models taking the bending stiffness of the reinforcement (Foraboschi, 2009) and the peeling stresses at the interface (Campi & Monetto, 2013) into account are available in the literature within the framework of two-layer beam structural models. Moreover, an approach directly connected to plated beams can be found in the recent paper by De Lorenzis et al. (2013). Of course such analytical treatments are much more onerous than the one provided in the present analysis and are generally not amenable to closed-form solutions.

The classical beam theory is exploited to model the beam. Referring to fig. 4a, the three equilibrium equations for the beam and the axial equilibrium equation for the reinforcement are:

$$\frac{\mathrm{d}T_\mathrm{b}}{\mathrm{d}z} = 0 \tag{11a}$$

$$\frac{\mathrm{d}N_\mathrm{b}}{\mathrm{d}z} - \tau\, t_\mathrm{r} = 0 \tag{11b}$$

$$\frac{\mathrm{d}M_\mathrm{b}}{\mathrm{d}z} - \frac{\tau\, h_\mathrm{b} t_\mathrm{r}}{2} - T_\mathrm{b} = 0 \tag{11c}$$

$$\frac{\mathrm{d}N_\mathrm{r}}{\mathrm{d}z} + \tau\, t_\mathrm{r} = 0 \tag{11d}$$

where T_b, N_b, M_b are the shear force, the axial force and the bending moment in the beam, N_r is the axial force in the FRP and τ is the interfacial shear stress. Note that, for the sake of simplicity, in order to have a positive solution for τ, the positive direction of the shear stresses is taken opposite to the usual one.

The axial force in the FRP vanishes at the plate end, providing the static boundary condition $N_\mathrm{r}(z_\mathrm{r}) = 0$. Thus, at $z = z_\mathrm{r}$, $M_\mathrm{b} = M = Pa/2$ and $T_\mathrm{b} = T = -P/2$. By means of these boundary conditions and eliminating τ from eqns (11), we achieve the following three relations between the internal reactions for $0 < z < z_\mathrm{r}$:

$$T_{\mathrm{b}} = -\frac{P}{2} \tag{12a}$$

$$N_{\mathrm{b}} + N_{\mathrm{r}} = 0 \tag{12b}$$

$$M_{\mathrm{b}} + \frac{N_{\mathrm{r}} h_{\mathrm{b}}}{2} = \frac{P}{2}(l - z) \tag{12c}$$

It is worth observing that these relations could have been derived directly from the scheme in fig. 4b, highlighting the static equivalence of the internal reactions for the overall composite beam and its constituents.

Eqns (11) represent a system of four equations in five unknowns: T_{b}, N_{b}, M_{b}, N_{r} and τ. Thus the problem is statically undetermined and for the solution we have to resort to kinematic and constitutive equations as well. Modelling the beam by the Timoshenko beam theory, these read respectively:

$$\gamma_{\mathrm{b}} = \frac{\mathrm{d}v_{\mathrm{b}}}{\mathrm{d}z} + \varphi_{\mathrm{b}} \tag{13a}$$

$$\varepsilon_{\mathrm{b}} = \frac{\mathrm{d}w_{\mathrm{b}}}{\mathrm{d}z} \tag{13b}$$

$$\chi_{\mathrm{b}} = \frac{\mathrm{d}\varphi_{\mathrm{b}}}{\mathrm{d}z} \tag{13c}$$

$$\varepsilon_{\mathrm{r}} = \frac{\mathrm{d}w_{\mathrm{r}}}{\mathrm{d}z} \tag{13d}$$

and

$$\gamma_{\mathrm{b}} = \frac{6}{5}\frac{T_{\mathrm{b}}}{G_{\mathrm{b}} t_{\mathrm{b}} h_{\mathrm{b}}} \tag{14a}$$

$$\varepsilon_{\mathrm{b}} = \frac{N_{\mathrm{b}}}{E_{\mathrm{b}} t_{\mathrm{b}} h_{\mathrm{b}}} \tag{14b}$$

$$\chi_{\mathrm{b}} = \frac{M_{\mathrm{b}}}{E_{\mathrm{b}} I_{\mathrm{b}}} \tag{14c}$$

$$\varepsilon_{\mathrm{r}} = \frac{N_{\mathrm{r}}}{E_{\mathrm{r}} t_{\mathrm{r}} h_{\mathrm{r}}} \tag{14d}$$

where v_{b}, w_{b} and φ_{b} are the transverse displacement, the axial displacement and the rotation of the beam cross section, while w_{r} is the axial displacement of the reinforcement; γ_{b} and ε_{b} are the shearing and axial strains of the beam; χ_{b} is the beam curvature, ε_{r} the axial strain of the reinforcement and G_{b} the shear elastic modulus of the beam material. Upon substitution of the constitutive eqns (14) and then of the kinematic eqns (13) into the equilibrium eqns (11), we obtain:

$$\frac{\mathrm{d}^2 v_{\mathrm{b}}}{\mathrm{d}z^2} + \frac{\mathrm{d}\varphi_{\mathrm{b}}}{\mathrm{d}z} = 0 \tag{15a}$$

$$\frac{\mathrm{d}^2 w_{\mathrm{b}}}{\mathrm{d}z^2} = \frac{t_{\mathrm{r}} \tau}{E_{\mathrm{b}} t_{\mathrm{b}} h_{\mathrm{b}}} \tag{15b}$$

$$\frac{\mathrm{d}^2\varphi_\mathrm{b}}{\mathrm{d}z^2} = \frac{t_\mathrm{r} h_\mathrm{b} \tau + 2T_\mathrm{b}}{2E_\mathrm{b} I_\mathrm{b}} \tag{15c}$$

$$\frac{\mathrm{d}^2 w_\mathrm{r}}{\mathrm{d}z^2} = -\frac{\tau}{E_\mathrm{r} h_\mathrm{r}} \tag{15d}$$

The problem can now be solved provided that the interfacial constitutive law $\tau = \tau(s)$ is assigned, s being the slip, i.e. the relative longitudinal displacement across the interface:

$$s = \left(w_\mathrm{b} + \varphi_\mathrm{b} \frac{h_\mathrm{b}}{2} \right) - w_\mathrm{r} \tag{16}$$

whose first derivative is, by means of eqns (13b,c,d) and eqns (14b,c,d):

$$\frac{\mathrm{d}s}{\mathrm{d}z} = \frac{1}{E_\mathrm{b}} \left(\frac{N_\mathrm{b}}{t_\mathrm{b} h_\mathrm{b}} + \frac{M_\mathrm{b}}{I_\mathrm{b}} \frac{h_\mathrm{b}}{2} \right) - \frac{N_\mathrm{r}}{E_\mathrm{r} t_\mathrm{r} h_\mathrm{r}} \tag{17}$$

Since the shear in the beam is known (see eqn (12a)), eqns (15) represent a system of 4 equations in the 4 displacement unknowns v_b, w_b, φ_b and w_r. However, if we derive twice eqn (16) and substitute eqns (15b,c,d), we obtain a second-order differential equation in a unique unknown, i.e. the relative displacement s:

$$\frac{\mathrm{d}^2 s}{\mathrm{d}z^2} - \frac{1 + 4\rho}{E_\mathrm{r} h_\mathrm{r}} \tau(s) = -\frac{3P}{t_\mathrm{b} h_\mathrm{b}^2 E_\mathrm{b}} \tag{18}$$

which represents the governing equation for the problem at hand. Note that eqn (15a) has not been exploited to achieve eqn (18), implying that the shear stress field along the interface is the same regardless whether the beam is modelled either as a Timoshenko or as a Euler-Bernoulli beam. This result is an outcome of the proposed modelling approach; beyond the TPB scheme, it holds true for any (externally) statically determinate geometry. In such cases the values of the internal reactions at the boundaries are known *a priori* and hence they can be used in eqn (15c), leading to eqn (18), and in eqn (17), providing the suitable boundary condition to integrate eqn (18) (see eqn (22) later). However, the coincidence of the interface shear stresses according to Timoshenko and Euler-Bernoulli beam models may be a more general feature, since, as shown in Wang et al. (2013), it holds true also for the Double Cantilever Beam geometry with an interface able to transfer both shear and peeling stresses.

Finally, it is worth observing that the shear deformability, while not affecting the interface stress field, does affect the mid-span deflection. However, we will neglect its contribution in Section 6, since our aim is to achieve a sufficiently simple analytical solution; thus, the complete analysis herein presented can be seen as limited to a Euler-Bernoulli beam model for the strengthened beam.

4. Interfacial cohesive law and dimensionless formulation

The interface is assumed to be macroscopically described by the τ vs. s function (cohesive law). Such a relation takes into account the shear deformability and the progressive damage mechanisms taking place both in the adhesive layer used to bond the FRP sheet to the substrate and in the superficial layer of the beam involved by the interfacial stress transfer (Ferracuti et al., 2006). Note that, for concrete beams, usually the debonding crack runs a few millimetres below the concrete

skin. Details of how to obtain the cohesive law starting from experimental tests can be found, e.g., in Carloni & Subramaniam (2010).

Although cohesive law featuring a power law (Ferracuti et al., 2007) or an exponential softening branch (Lu et al., 2005) can be more realistic, aiming at a closed-form analytical solution we assume herein that the mechanical behaviour of the interface can be satisfactorily described by a bi-linear law as represented in fig. 5. The interfacial law is completely defined by means of three parameters, e.g. the peak stress τ_p, the corresponding relative displacement s_p and the final relative displacement s_f, i.e. the value after which the reinforcement is considered completely detached from the beam. The initial (elastic) stiffness of the interface is denoted by $k = \tau_p / s_p$ and the interfacial fracture energy is equal to $\mathcal{G}_c = \tau_p s_f / 2$. Introducing the ratio $\mu = s_f / s_p$ and the normalized relative displacement $\delta = s / s_p$, the cohesive law can be given in a dimensionless form as:

$$\frac{\tau}{\tau_p} = f(\delta) = \begin{cases} \delta, & \text{if } 0 \le \delta \le 1 \\ \dfrac{\mu - \delta}{\mu - 1}, & \text{if } 1 < \delta \le \mu \\ 0, & \text{if } \delta > \mu \end{cases} \tag{19}$$

In this dimensionless form, the interface law depends only on the parameter $\mu \ge 1$, ruling the interface brittleness/ductility. While for $\mu = 1$ the interface shows an elastic-perfectly brittle behaviour, for $\mu \to \infty$ the cohesive behaviour turns into an elastic-perfectly plastic one.

In order to simplify the analytical manipulations and, at the same time, to highlight the parameters affecting the structural behaviour, it is convenient to give a dimensionless formulation to the governing equation (18). Lengths are most conveniently normalized with respect to the characteristic length l_{ch} defined as:

$$l_{ch} = \sqrt{\frac{E_r h_r}{k(1+4\rho)}} \tag{20}$$

Note that l_{ch} depends only on the geometry and elastic properties of the constituent materials. Dimensionless quantities, whenever possible, are represented by the corresponding Greek symbol. Thus the dimensionless longitudinal coordinate, reinforcement length, length of the unreinforced region and beam span (see fig. 2) are given by $\zeta = z / l_{ch}$, $\zeta_r = z_r / l_{ch}$, $\alpha = a / l_{ch}$, $\lambda = l / l_{ch}$, respectively. The load is normalized with respect to the Jourawsky estimate (eqn (6)), i.e. $\Pi = P / P_{Jou}$. By means of these new quantities, eqn (18) simplifies into:

$$\frac{d^2\delta}{d\zeta^2} - f(\delta) = -\Pi \tag{21}$$

5. Analysis of the debonding process

In this section we analyze the evolution of the stress and relative displacement fields along the interface during the debonding process. This process consists of three stages: the elastic stage, the elastic-softening stage and the elastic-softening-debonding stage.

5.1 Elastic stage

During the first stage the whole length of the interface is in the elastic regime ($\delta < 1$) and the controlling parameter is the load which increases from 0 up to a limit value. Boundary conditions prescribe a null relative displacement at the mid-span (because of symmetry) as well as a vanishing axial stress in the reinforcement at its edge, i.e. $N_r = 0$ at $z = z_r$. As already observed in Section 3, this implies $N_b = 0$ and $M_b = M = Pa/2$ at $z = z_r$, so that from eqn (17) we obtain:

$$\left.\frac{\mathrm{d}s}{\mathrm{d}z}\right|_{z=z_r} = \frac{3Pa}{E_b t_b h_b^2} \tag{22}$$

In dimensionless form, the mathematical problem reads:

$$\begin{cases} \delta'' - \delta = -\Pi\,, \quad 0 \le \zeta \le \zeta_r \\ \delta(0) = 0 \\ \delta'(\zeta_r) = \Pi\alpha \end{cases} \tag{23}$$

where the prime denotes derivation with respect to ζ. The solution is:

$$\delta(\zeta) = \frac{\tau}{\tau_p}(\zeta) = \Pi\left[1 + \frac{\alpha \sinh \zeta - \cosh(\zeta_r - \zeta)}{\cosh\zeta_r}\right] \tag{24}$$

reaching the maximum value at the edge:

$$\delta(\zeta_r) = \frac{\tau}{\tau_p}(\zeta_r) = \Pi\left(1 + \alpha \tanh \zeta_r - \mathrm{sech}\zeta_r\right) \tag{25}$$

Note that, in view of the mode II debonding crack that will grow starting from $\zeta = \zeta_r$, the relative displacement given by eqn (25) can be seen as the dimensionless Crack Mouth Sliding Displacement (CMSD). In this first stage it is lower than unity.

As expected, in the elastic regime the solution is proportional to the load Π. The other parameters affecting the solution are α and ζ_r or, equivalently, the normalized length λ ($\lambda = \alpha + \zeta_r$) and the relative reinforced length $\zeta_r / \lambda = z_r / l$. The shear stress field is plotted in fig. 6 (for $\lambda = 20$ and a relative reinforced length z_r / l equal to 0.8) at the end of the elastic stage, i.e. when the stress at the FRP edge reaches its peak value τ_p (i.e. $\delta = 1$). It is here interesting to observe that far away from the FRP edges and from the mid-span, the shear stress tends to be constant and equal to the EB solution, i.e. $\tau = \tau_{Jou}$. In other words, taking the interface compliance into account highlights the presence of two boundary layers: the first one at mid-span, providing the transition to a vanishing shear stress on the axis of symmetry; the second at the reinforcement edge, describing the stress concentration which triggers the debonding crack. For a given relative reinforced length, the higher is λ, the narrower the boundary layers and the stronger the stress concentration. In the limit case of perfect interfaces (i.e. $k \to \infty \Rightarrow \lambda \to \infty$), the shear stress at the FRP edge diverges, while the quantity $\tau^2(z_r)/2k$ remains finite, tending to the strain energy release rate $\mathcal{G}$ provided by the LEFM-EB model (i.e. eqn(8), see also Carpinteri et al. (2009b)).

5.2 Elastic-softening stage

The elastic stage ends when the shear stress reaches its peak value at the FRP edge, i.e. $\delta(\zeta_r) = 1$. Equation (25) provides the corresponding limit elastic load value:

$$\Pi_{el} = (1 + \alpha \tanh \zeta_r - \operatorname{sech}\zeta_r)^{-1} \tag{26}$$

Beyond this value, part of the interface begins to soften. In order to analyze the debonding process, the controlling parameter is now the position $\zeta = \overline{\zeta}$ of the fictitious crack tip, i.e. the position of the shear stress peak, which starts travelling from the FRP edge towards the midspan. In the range (0, $\overline{\zeta}$), the interface is still in the elastic regime. Hence the stress field here is obtained by solving the following differential problem:

$$\begin{cases} \delta'' - \delta = -\Pi, \quad 0 \le \zeta \le \overline{\zeta} < \zeta_r \\ \delta(0) = 0 \\ \delta(\overline{\zeta}) = 1 \end{cases} \tag{27}$$

whose solution reads:

$$\delta(\zeta) = \frac{\tau}{\tau_p}(\zeta) = \frac{\sinh \zeta}{\sinh \overline{\zeta}} + \Pi \left\{ 1 - \frac{\sinh \zeta + \sinh(\overline{\zeta} - \zeta)}{\sinh \overline{\zeta}} \right\}, \; 0 \le \zeta \le \overline{\zeta} \tag{28}$$

In the so-called process zone $\overline{\zeta} < \zeta < \zeta_r$ the form of the differential equation changes, since the function f to be inserted into eqn (21) is now given by the softening branch (see eqn (19)). Therefore:

$$\begin{cases} \delta'' - (\mu - \delta)/(\mu - 1) = -\Pi, \quad 0 < \overline{\zeta} \le \zeta \le \zeta_r \\ \delta(\overline{\zeta}) = 1 \\ \delta'(\zeta_r) = \Pi\alpha \end{cases} \tag{29}$$

The solution reads:

$$\delta(\zeta) = \mu - (\mu - 1) \frac{(1 - \Pi) \cos\mu_2(\zeta_r - \zeta) + \Pi \left[\cos\mu_2(\zeta_r - \overline{\zeta}) - \alpha\mu_2 \sin\mu_2(\zeta - \overline{\zeta}) \right]}{\cos\mu_2(\zeta_r - \overline{\zeta})}, \; \overline{\zeta} \le \zeta \le \zeta_r \tag{30}$$

where the parameter $\mu_2 = (\mu - 1)^{-1/2}$ has been introduced for the sake of simplicity. The corresponding CMSD is:

$$\delta(\zeta_r) = \mu - (\mu - 1) \left\{ (1 - \Pi) \sec\mu_2(\zeta_r - \overline{\zeta}) + \Pi \left[1 - \alpha\mu_2 \tan\mu_2(\zeta_r - \overline{\zeta}) \right] \right\} \tag{31}$$

In this second stage it is $1 \le \delta \le \mu$. Once substituted into eqn (19), eqn (30) provides also the shear stress field in the process zone:

$$\frac{\tau}{\tau_p}(\zeta) = \frac{(1 - \Pi) \cos\mu_2(\zeta_r - \zeta) + \Pi \left[\cos\mu_2(\zeta_r - \overline{\zeta}) - \alpha\mu_2 \sin\mu_2(\zeta - \overline{\zeta}) \right]}{\cos\mu_2(\zeta_r - \overline{\zeta})}, \; \overline{\zeta} \le \zeta \le \zeta_r \tag{32}$$

Eqn (32) does not define completely the solution since the load is yet to be determined. Its value can be found through a continuity condition at the boundary between the elastic and the softening

regions. In fact, since the internal reactions are continuous across the beam length, the first derivative of the slip must be continuous as well (see eqn (17)). This implies that:

$$\delta'(\overline{\zeta}^{+}) = \delta'(\overline{\zeta}^{-}) \tag{33}$$

Upon substitution of the solution of eqn (27) and (29) into eqn (33), we get the desired value for the load:

$$\Pi = \left\{ 1 + \frac{\alpha \sec[\mu_2(\zeta_r - \overline{\zeta})] - \operatorname{csech} \overline{\zeta}}{\sqrt{\mu - 1} \tan[\mu_2(\zeta_r - \overline{\zeta})] + \operatorname{ctanh} \overline{\zeta}} \right\}^{-1} \tag{34}$$

and the solution is now complete.

5.3 Elastic-softening-debonding stage

The second stage ends when the CMSD at the FRP edge reaches the value s_f. Beyond this value, the external part of the reinforcement completely detaches from the support and a real crack tip appears behind the fictitious crack tip.

In dimensionless form, the condition defining the beginning of debonding is $\delta(\zeta_r) = \mu$. According to eqn (31) and (34), this condition is met when the position $\overline{\zeta}$ of the peak stress is the root of the following equation:

$$\alpha \mu_2 \sin[\mu_2(\zeta_r - \overline{\zeta})] - \cos[\mu_2(\zeta_r - \overline{\zeta})] = \frac{\alpha \sec[\mu_2(\zeta_r - \overline{\zeta})] - \operatorname{csech} \overline{\zeta}}{\sqrt{\mu - 1} \tan[\mu_2(\zeta_r - \overline{\zeta})] + \operatorname{ctanh} \overline{\zeta}} \tag{35}$$

where, in case of multiple roots, the largest value has to be taken. We denote such a root with $\overline{\zeta}_{23}$, since it is the location of the fictitious crack tip at which the second stage ends and the third one begins.

During the elastic-softening-debonding stage, the position of the real crack tip, which is now most conveniently chosen as the controlling parameter, moves gradually from the FRP edge towards the mid-span. However it is not necessary to solve any additional differential problem, since the solution is the same as in a strengthened beam of reduced reinforced length at the end of the second stage. Hence, from a computational point of view, the solution during the third and last stage is still given by the equations valid for the second stage: the difference is that now ζ_r varies from the initial value to 0; meanwhile, the corresponding position of the fictitious crack tip, varying from $\overline{\zeta}_{23}$ to 0, is obtained by solving eqn (35) for each ζ_r value. Finally, simple beam theory leads to the expression for the CMSD (larger than μ) during this last stage as:

$$\delta(\zeta_r) = \mu + \Pi\left(\zeta_{r,0} - \zeta_r\right)\left(\lambda - \frac{\zeta_{r,0} + \zeta_r}{2}\right) \tag{36}$$

where $\zeta_{r,0}$ is the original (normalized) reinforced length.

Once the shear stress at the interface is known, the axial equilibrium equation (11d) of the reinforcement delivers the normal stress in the FRP plate. Explicit expressions are provided in Appendix A.

In summary, the normalized shear stress at the interface and normal stress in the FRP depend only on three dimensionless parameters: the normalized length λ, the relative reinforced length z_r/l

and the parameter μ, ruling the interfacial brittleness/ductility. In figs. 7 and 8 the stress fields are plotted at different stages of the debonding process for $\lambda = 20$, $z_r/l = 0.8$ (i.e. $\zeta_r = 16$) and $\mu = 5$. As representative of the debonding growth, we consider the end of the elastic stage, the attainment of the (relative) maximum load, the beginning of the detachment, and a detached length equal to 25%, 50% and 75% of the initial reinforced length, respectively. Fig. 7 shows the shear stress field at the different stages, highlighting the positions of the fictitious and real crack tips (corresponding respectively to the peak and to the zero shear stress) and how they move towards the mid-span, while fig. 8 shows the axial stress in the FRP plate at the same stages. Note that the central portion of the interface, where $\delta = 0$ because of symmetry, always remains in the elastic regime. The region where the interfacial shear stress is constant and the FRP normal stress is linear defines the zone where EB theory can be used to compute the stresses. Finally, as far as the stress at the maximum load is concerned (dashed lines), it should be observed that the highest load value occurs during the second stage. As will be shown in the following section, however, there are values of the parameters for which the load is monotonically increasing during debonding, i.e. no maximum occurs.

6. Structural response

Tests on plated beams are usually displacement-controlled. It is therefore interesting to derive also the analytical expression for the displacements and, particularly, for the mid-span deflection. In order to obtain a closed-form expression, herein we assume that the beam can be satisfactorily described as a Euler-Bernoulli beam. This assumption is equivalent to neglecting the shear deformability, so that eqn (13a) yields $\varphi_b = -\mathrm{d}v_b/\mathrm{d}z$. Substituting this relation into eqn (15c) leads to:

$$\frac{\mathrm{d}^3 v_b}{\mathrm{d}z^3} = \frac{P - t_r h_b \tau}{2 E_b I_b} \tag{37}$$

Before integrating eqn (37), it is convenient to substitute the shear stress on the right-hand side with its expression obtained from the governing equation (18). Thus we obtain:

$$\frac{\mathrm{d}^3 v_b}{\mathrm{d}z^3} = \frac{P}{2 E_b I} - \frac{6\rho}{1+4\rho}\frac{1}{h_b}\frac{\mathrm{d}^2 s}{\mathrm{d}z^2} \tag{38}$$

Note that, up to the last term, eqn (38) represents the Euler-Bernoulli equation for a beam reinforced over the whole span according to the EB model. Integrating three times eqn (38), exploiting the proper boundary conditions and evaluating the deflection at the mid-span yields:

$$v_b(0) = v = \frac{P(2l)^3}{48 E_b I} + \frac{6\rho}{(1+4\rho)h_b}\int_0^l s(z)\,\mathrm{d}z \tag{39}$$

where, according to what already observed for eqn (38), the first term on the right-hand side represents the mid-span deflection for a beam reinforced over the whole span using the EB model. Note that a beam whose reinforced length is lower than the beam span can be seen as a beam reinforced over the whole length but whose FRP plate is detached at the edges. This trick allows us to give a meaning to the relative displacement s also in the range $z_r < z < l$, where it is equal to its value at the edge ($z = z_r$) plus the integral of the strain on the soffit of the beam. Consequently, eqn (39) can be cast as:

$$v = v_{EB} + \frac{6\rho}{(1+4\rho)h_b}\left[\int_0^{z_r} s(z)\,dz + (l - z_r)\,s(z_r)\right] \tag{40}$$

where the first term represents the mid-span deflection according to the EB model, already provided in eqn (10), and the second term represents the additional contribution due to the interface compliance, which coherently vanishes for $s \equiv 0$, i.e. for an infinitely stiff (perfect) interface. By normalizing the displacements with respect to the mid-span deflection v_{Jou} of an unreinforced beam at $P = P_{Jou}$:

$$v_{Jou} = \frac{P_{Jou}(2l)^3}{48E_bI_b} \tag{41}$$

eqn (40) can be rewritten as:

$$\frac{v}{v_{Jou}} = \frac{\Pi\left[(1+\rho)\lambda^3 + 3\rho\alpha^3\right] + 9\rho\left[\int_0^{\zeta_r} \delta(\zeta)\,d\zeta + \alpha\,\delta(\zeta_r)\right]}{(1+4\rho)\lambda^3} \tag{42}$$

In eqn (42), the normalized values of the load (Π) and of the slip at the edge ($\delta(\zeta_r)$) during debonding are given by eqns (34) and (31) respectively, while the integral can be evaluated analytically and it is provided explicitly in Appendix B.

Before analyzing a typical load vs. displacement curve, it is worth observing that, unlike the interfacial shear stress field, the structural behaviour depends not only on the three parameters λ, ζ_r and μ, but also explicitly on the reinforcement ratio ρ, given by eqn (1). In particular, the reinforcement ratio rules the difference between the slope at the beginning and at the end of the test, whereby the former represents the stiffness of the reinforced, undamaged structure and the latter is the stiffness of the unreinforced structure, set equal to one according to the normalization adopted. For the sake of clarity, in the following, we have chosen relatively high ρ values to provide more easily readable plots.

In fig. 9, the load vs. mid-span deflection plot has been drawn for $\lambda = 10$, $\zeta_r = 7$, $\mu = 5$ and $\rho = 0.4$, along with the prediction based on LEFM. The elastic stage is represented by a straight green line, whose slope is only slightly lower than the LEFM curve since the model takes also the elastic interface compliance into account. At point A the interface enters the elastic-softening stage and non-linearity in the load vs. displacement curve appears. This second stage is represented by the blue portion of the curve, from point A to point B. For usual values of the parameters, during the second stage the curve shows a local maximum P_{max}, after which the load starts to soften, in the present case with a positive slope in the load vs. displacement plot. It is worth observing that the maximum load is usually significantly larger than the limit elastic load P_{el} (about twice in the present case), thus proving the need for the present non-linear analysis. On the other hand, P_{max} is usually significantly smaller than the predictions based on LEFM and Jourawsky's formula (P_{LEFM} and P_{Jou}, respectively), the latter one being represented by unity on the vertical axis. This proves that the uncritical use of the debonding load estimates (6) and (9) is potentially dangerous and justifies once more the need for the present approach.

At point B the detachment of the reinforcement from the support starts from the edge of the FRP plate and the interface enters the elastic-softening-debonding (third) stage (red part). The debonding crack runs fast towards the beam mid-span and only at the end it slows down. Note that in the present quasi-static analysis, the velocity of the debonding is not referred to time but to the test

control parameter: we mean that a variation of the mid-span deflection (or of the CMSD, see below) causes a large growth of the debonding crack at the beginning of the third stage and a small growth towards the end, as clearly shown by the black dots in fig.9, corresponding to equispaced positions of the real crack tip. At the very end, large increments of the load (or of the mid-span displacement) are required to have a further debonding growth, but the reinforcement is almost completely detached, so that the curve approaches the straight line representing the linear-elastic behaviour of the unreinforced beam.

It is interesting to observe that the present model includes, for $\mu = 1$, the case of a linear elastic-perfectly brittle interface analyzed in Carpinteri et al. (2009b) (see also Távara et al. (2011) for applications to other geometries and mixed mode interface crack propagation). In such a case the load vs. deflection plot shows always an angular point at beginning of debonding, while the behavior becomes smooth for μ larger than unity. If, beyond $\mu = 1$, we assume a perfect interface (i.e. infinitely stiff, $k \to \infty$), both λ and ζ_r tend to ∞ (while their ratio keeps constant and equal to the relative bond length) and the model prediction reverts to the LEFM-EB model solution provided in Section 2, which, therefore, can be seen as a limit case of the present, more general approach.

From fig. 9 it is evident that, if the test is load-controlled, a snap-through instability occurs, i.e. a sudden displacement jump from the point where the load attains its local maximum to the final branch. For a softening branch with positive slope, a snap-back instability occurs also in case of mid-span deflection-controlled tests, i.e. a sudden load drop down to the bottom branch of the curve is obtained. In both cases the unstable behaviour yields an amount of energy that exceeds the one needed to detach the corresponding portion of the reinforcement from the substrate; thus it involves dynamic effects typically leading to a catastrophic failure with the sudden detachment of the complete FRP plate (see e.g. Pellegrino & D'Antino, 2013). On the other hand, if a test control can be chosen which is able to avoid dynamic effects (see the later discussion), the complete detachment of the reinforcement theoretically occurs only at infinite load.

Although for typical values of λ, μ, ζ_r both snap-back and snap-through instabilities may occur (depending on the test controlling parameter), there are also values for which one or both of the instabilities disappear. Accordingly, three types of structural behaviour can be identified, as illustrated in fig. 10. Here the load vs. mid-span deflection curves are drawn for different values of the parameters: in fig. 10a $\lambda = 11$, $\mu = 12$, $\zeta_r / \lambda = 0.8$ and both instabilities may occur; in fig. 10b $\lambda = 10$, $\mu = 15$, $\zeta_r / \lambda = 0.75$ and only snap-through instability may take place; in fig. 10c $\lambda = 9$, $\mu = 18$, $\zeta_r / \lambda = 0.7$ and instabilities are inhibited. As expected, the brittle-to-ductile transition occurs as the structural size decreases (low λ values), as the interface ductility increases (high μ values), and as the relative reinforcement length decreases (low ζ_r / λ values).

Note that large λ values can be achieved not only for large sizes, but also for small mechanical reinforcement percentage or large interface stiffness according to the l_{ch} definition (eqn (20)). However, care must be adopted when addressing the effects of the parameters k and ρ on the structural response, since k affects also the μ value (see eqn (51) later) and ρ affects also the mid-span displacement values (see eqn (42)).

Since the solution basically depends on three parameters, by fixing one of them it is possible to construct two-dimensional maps highlighting the regions where instabilities are expected. An example of such maps is provided in fig. 11, where the relative reinforcement length is set equal to the typical value 0.8. According to the μ- and λ-values, both, one or no instability may occur. As expected, the structural behaviour tends to be catastrophic for large sizes (high λ) and brittle interfaces (low μ). Finally observe that the contour of the region where the snap-back instability is present depends, although weakly, also on the parameter ρ (set equal to 0.125 in fig. 11).

If it is desired to follow also the softening branch with positive slope in the load vs. mid-span displacement plot, a controlling parameter different from both load and displacement is required. Carpinteri (1989), analyzing the structural behaviour of cracked TPB specimens (mode I loading), observed that the Crack Mouth Opening Displacement (CMOD) is monotonically increasing during

the test. Analogously, for the mode II problem at hand herein, we can choose as the control parameter the CMSD, i.e. the relative sliding displacement between the FRP strip and the support at the termination of the strengthening plate. By means of eqns (25), (31) and (36) it is possible to plot the load vs. CMSD curve. In fig. 12a,b,c the curves are obtained for the same values used for fig. 10. It is evident that the CMSD, differently from the mid-span deflection, is always monotonically increasing. This different behaviour is highlighted in fig. 12d, where the curves provided in fig. 10a and 12a are compared.

7. Computation of the maximum load

In the previous sections we have seen that usually during the debonding process the load shows a local maximum. The computation of this value is very important, especially because in practice the maximum is not local but absolute, since the final, never-ending ascending branch in the load vs. displacement plot is here obtained under the unrealistic assumption of an infinitely resistant linear elastic behaviour for the beam.

Wishing to determine the maximum load and the corresponding extension of the process zone, we can proceed from the analytical computations of Section 5. If a maximum is to be achieved, this is reached in the elastic-softening stage, when the load is given by eqn (34) as a function of the position of the stress peak $\overline{\zeta}$. The stationary point is thus determined by setting:

$$\frac{\mathrm{d}\,\Pi}{\mathrm{d}\,\overline{\zeta}} = 0 \tag{43}$$

After some analytical manipulations we obtain:

$$\tanh \overline{\zeta}\, \tan[\mu_2(\zeta_r - \overline{\zeta})] = \sqrt{\mu - 1} \tag{44}$$

whose root $\overline{\zeta} = \overline{\zeta}_{max}$, if existing, defines the (normalized) position of the fictitious crack tip at which the load reaches its (normalized) maximum value Π_{max} and the corresponding extension of the (normalized) process zone $(\zeta_r - \overline{\zeta}_{max})$. Interestingly, this value depends only on μ and ζ_r and not on λ. Furthermore, it is worth noting that eqn (44) is formally similar to the equation providing the amplitude of the process zone at maximum load in direct shear tests (Yuan et al., 2004).

Eqn (44) is a transcendental equation that has to be solved numerically. Once the value $\overline{\zeta}_{max}$ is computed, the maximum load is obtained by its substitution into eqn (34). By means of eqn (44), the expression for the normalized debonding load can be simplified as:

$$\Pi_{max} = \frac{\mu}{\mu - \operatorname{sech} \overline{\zeta}_{max} + \alpha\sqrt{\mu - \operatorname{sech}^2 \overline{\zeta}_{max}}} \tag{45}$$

which, multiplied by P_{Jou}, provides the maximum load P_{max}.

Usually, the distance between the position of the fictitious crack tip at maximum load and the beam mid-span is much larger than the characteristic length l_{ch}, i.e. $\overline{\zeta}_{max} >> 1$. Thus the hyperbolic tangent in eqn (44) and the hyperbolic secant in eqn (45) can be set equal to unity and to zero, respectively, leading to the following simplified expressions for the process zone and for the maximum load:

$$z_r - z_{max} \cong l_{ch}\left(\sqrt{\mu - 1}\ \ \text{atan}\sqrt{\mu - 1}\right) \tag{46}$$

$$P_{max} \cong \frac{P_{Jou}}{1 + \alpha/\sqrt{\mu}} \tag{47}$$

From eqns (6) and (9) it is easy to check that the ratio of the Jourawsky's to the LEFM estimate of the debonding load is equal to:

$$\frac{P_{Jou}}{P_{LEFM}} = \frac{\alpha}{\sqrt{\mu}} \tag{48}$$

Thus eqn (47) can be also rewritten as:

$$P_{max} \cong \frac{P_{LEFM}}{1 + \sqrt{\mu}/\alpha} \tag{49}$$

whereas eqn (26), under the same assumptions, reads:

$$\frac{P_{el}}{P_{Jou}} \cong \frac{1}{1 + \alpha} \quad \Rightarrow \quad P_{max} \cong \frac{1 + \alpha}{1 + \alpha/\sqrt{\mu}} P_{el} \tag{50}$$

Equation (46) shows that the process zone is typically given by the characteristic length l_{ch} times a factor increasing with the ductility of the interface (i.e. with μ). On the other hand, in eqns (47) and (49) the denominators are larger than unity, thus showing that usually the predictions based on Jourawsky's formula and LEFM overestimate the maximum load, while eqn (50) shows that the limit elastic load underestimates the maximum load. Note that for high α values (e.g. large sizes or small reinforcements) the maximum load tends to the LEFM estimate. However, it is worth observing that care must be adopted when using these simplified expressions (eqns 46-50) since, for a relatively large process zone, they become less and less accurate, finally becoming physically meaningless when eqn (44) admits no roots and the load becomes monotonically increasing during the delamination.

The ratio $\alpha/\sqrt{\mu}$ does not depend on the interfacial elastic stiffness k. This feature can be easily checked noting that the parameter μ can be expressed in terms of k, $\mathcal{G}_c$ and τ_p as:

$$\mu = \frac{2\, k\, \mathcal{G}_c}{\tau_p^2} \tag{51}$$

whereas α is equal to the ratio of a to l_{ch}, whose expression is given by eqn (20). Therefore, as long as the approximation $\overline{\zeta}_{max} >> 1$ holds true, we can conclude that the elastic stiffness k of the interface has a negligible influence on the maximum load, a feature that is quite commonly observed in cohesive zone modeling. The explicit expression of the debonding load provided by eqn (47) is:

$$P_{max} \cong \frac{1 + 4\rho}{3\rho} \tau_p t_r h_b \left(1 + \tau_p a \sqrt{\frac{1 + 4\rho}{2 E_r h_r \mathcal{G}_c}}\right)^{-1} \tag{52}$$

and it was originally derived in De Lorenzis & Zavarise (2009).

The last part of the present section is devoted to the computation of the failure load estimate provided by the Finite Fracture Mechanics, which, essentially, is a fracture criterion resting on the assumption of a finite crack advancement (Cornetti et al., 2006). The length Δ of such advancement is determined by fulfilling the energy balance and a suitable stress requirement. While the theoretical bases of the CCM and of the FFM are distinct, the maximum load estimates provided by the two approaches are usually in excellent agreement (Henninger et al., 2007); on the other hand, requiring only the elastic solution, the FFM failure load estimate is much easier to achieve.

Regarding the stress condition, we require the average stress to be equal to the peak strength τ_p over the crack extension, i.e.:

$$\int_{z_r-\Delta}^{z_r} \tau(z)\,\mathrm{d}z = \tau_p \Delta \tag{53}$$

Differently from the CCM, it is evident from eqn (53) that FFM allows the shear stress to overcome the shear strength in the neighbourhood of the crack tip. By means of eqn (24), eqn (53) in dimensionless form reads:

$$\Pi \int_{\zeta_r-\xi}^{\zeta_r} \left[1+\frac{\alpha \sinh\zeta - \cosh(\zeta_r-\zeta)}{\cosh\zeta_r}\right] \mathrm{d}\zeta = \xi \tag{54}$$

where ξ is the normalized crack advancement Δ / l_{ch}. The integral in eqn (54) can be easily calculated in closed form: its explicit expression is given in Appendix C.

As far as the energy balance is concerned, we observe that, for elastic interfaces, the strain energy release rate $\mathcal{G}$ is simply given by $\tau^2(z_r)/2k$ (Carpinteri et al., 2009b). Hence, the energy balance for a finite crack extension requires that (Cornetti et al., 2012):

$$\int_{z_r-\Delta}^{z_r} \frac{\tau^2(z_r')}{2k}\,\mathrm{d}z_r' = \mathcal{G}_c \Delta \tag{55}$$

By means of eqn (25), eqn (55) in dimensionless form reads:

$$\Pi^2 \int_{\zeta_r-\xi}^{\zeta_r} \left[1+(\lambda-\zeta_r')\tanh\zeta_r' - \operatorname{sech}\zeta_r'\right]^2 \mathrm{d}\zeta_r' = \mu\xi \tag{56}$$

The integral in eqn (56) can be easily calculated in closed form: its explicit expression is given in Appendix C as well. Eqns (53) and (55) (i.e. (54) and (56)) represent a system of two equations in two unknowns: the finite crack advancement and the debonding load. Obtaining the load Π from eqn (54) and substituting it into eqn (56) yields a unique equation in the unique unknown ξ. Its root has to be obtained numerically. Then eqn (54) (or eqn(56)) provides the debonding load.

As far as the maximum load is concerned, it is evident that FFM is much easier to apply with respect to the CCM, since FFM requires only the elastic solution of Section 5.1. In the present case, however, the CCM solution has been obtained analytically: therefore, the FFM estimate of the debonding load has only the goal of validating the FFM criterion by comparison with the widely established CCM approach.

In fig. 13 we plot the debonding load vs. the interface ductility (represented by the parameter μ) for different values of the dimensionless beam span (i.e. λ = 5, 10, 15) and a fixed value of the

relative reinforcement length (i.e. $z_r/l = 0.8$) according to LEFM, FFM, CCM and approximate CCM (i.e. eqn (47)). It is clear that LEFM largely overestimates the debonding load. On the other hand FFM follows the same trend provided by the more refined CCM, with a relative difference of few unit percent for relatively brittle interfaces ($\mu \lesssim 10$). The approximate expression provided by eqn (47) turns out to be very accurate, showing some non-negligible differences only for the lowest λ value. As already observed, above a threshold μ value (depending on λ as well), the maximum disappears so that the CCM does not provide a solution anymore. It is worth observing that the same occurs for the FFM criterion, where the equation providing the crack advancement admits no roots for slightly larger threshold μ values. Of course this fact does not mean that debonding does not occur in this less common case, but the FFM solution has a different form. For details see Mantič (2009), where this latter case is referred to as ‘‘scenario B’’.

8. Parametric analysis

We conclude the paper with a parametric analysis. We start by considering a specific case, with the following geometry and material properties: $l = 1000$ mm; $z_r = 800$ mm; $h_b = 200$ mm; $h_r = 5$ mm; $t_b = t_r = 100$ mm; $E_b = 30$ GPa; $E_r = 240$ GPa; $\tau_p = 4$ MPa; $s_p = 0.06$ mm; $s_f = 0.6$ mm. We denote this geometry as the reference case. Then we will modify some geometry or material features and highlight how they affect the structural response. The load vs. displacement curves referring to the reference case are plotted in a thicker line in the following figures.

In fig. 14 the effect of the stiffness E_r of the reinforcement is considered. We introduce the parameter n defining the ratio of the Young’s moduli of the reinforcement and the beam materials. This is equal to 8 for the reference case; in fig. 14 it varies from 4 to 12. Note that, for the sake of clarity, in fig. 14 (as well as in the following ones) the load and the mid-span displacement are normalized with respect to quantities which are not affected by the parameter that has to be varied, n in the present case (while the previous normalizing quantities P_{Jou} and v_{Jou} do depend on E_r). Fig. 14 clearly shows that the higher is the FRP stiffness, the steeper is the initial slope and the lower the maximum load. On the other hand, very brittle behaviours are expected for relatively low n ratios. Note that the area between the different curves and the straight dashed line (representing the behaviour of the unreinforced beam) is the same for all the curves, since, up to a multiplicative constant, is proportional to the energy spent to detach the FRP plate from the support.

In fig. 15 we consider a first effect of the interface law: we keep τ_p and k constant and let μ vary from 1 (elastic-perfectly brittle case) to ∞ (elastic-perfectly plastic), see fig. 15a. From fig. 15b it is evident that the brittleness decreases as μ increases. The area between the curves and the short-dashed line increases since the fracture energy increases along with μ. Finally the long-dashed line represents the structural behaviour of a beam subjected (beside the external load) to a uniform (and equal to τ_p) distribution of shear stresses along the reinforcement length. The corresponding equation is provided in Appendix D. As expected, the long-dashed line represents the asymptote for sufficiently large loads of the elastic-perfectly plastic case.

A second effect of the interface law is shown in fig. 16. In this case we keep constant $\mathcal{G}_c$ and k while letting μ vary from 2 to 20, see fig. 16a. As in the previous case, the brittleness decreases as μ increases (fig. 16b): the maximum load decreases as well, finally disappearing for μ equal to 20, when the load becomes monotonically increasing with the mid-span deflection. On the other hand, differently from what observed for fig. 15 (and analogously to fig. 14), the area between the different curves and the straight dashed line is the same for all the curves.

In fig. 17 we analyze the so-called size effect: with respect to the reference case, we scale all the geometry values by a factor ranging from 0.25 up to 4 (i.e. h_b varies from 50 mm up to 800 mm). Note that, although the material and the interface properties are kept constant, the structural behaviour changes dramatically, ranging from very brittle for the largest size to highly ductile for

the smallest one. It is worth noting that, as long as the ratios E_r/τ_p, E_b/τ_p and μ are kept constant, increasing the strength, increasing the overall structural size or decreasing the fracture energy has the same effect on the structural response, so that the structural behaviour is identified by the (energetic) brittleness number s_E defined as:

$$s_E = \frac{\mathcal{G}_c}{\tau_p h_r} \tag{57}$$

The definition of brittleness number provided by eqn (57) represents the straightforward generalization to a mode II debonding problem of the definition provided by Carpinteri (1982) for mode I geometries. According to eqn (57), the curves in fig. 17 correspond to brittleness numbers ranging from 0.015 up to 0.24. Note that in fig. 17 the load and displacement values have been normalized with respect to quantities scaling with the structural size. Since the normalized maximum load in fig. 17 is decreasing with increasing size, it means that the actual debonding load increases with the size according to an exponent lower than 2 (but higher than 1.5, i.e. the value predicted by LEFM, see eqn(9)).

Finally we consider how the relative reinforcement length affects the structural behaviour. As fig. 18 evidences (and as expected), there is a clear advantage in prescribing large bond lengths; however care must be paid since, along with a drastic increment of the debonding load, the structural response becomes more and more catastrophic. Note that the area between the different curves and the straight dashed line is not the same since, although $\mathcal{G}_c$ is the same for all the cases, the area subjected to debond changes from geometry to geometry. A confirmation of these predictions is provided by the experimental tests performed by Büyüközturk et al. (1998), who, testing four-point bending plated beams with different reinforcement lengths, observed a decrease of the maximum load as well as the disappearance of both the snap-back and snap-through instabilities for the shorter FRP plates. Both these features are correctly taken into account by the present model.

9. Conclusions

In this paper we presented an analytical approach for the prediction of the edge debonding of a thin FRP plate from the soffit of a beam. The approach is based on the cohesive crack modelling of the interface between the FRP and the support; moreover, it is assumed that only shear stresses are transmitted across the interface. The analysis is an extension of previous results of the authors (Carpinteri et al., 2009b; De Lorenzis & Zavarise, 2009), the main novelty being a detailed parametric analysis of the structural response along with an almost closed form solution for the maximum load.

The load vs. mid-span deflection and the load vs. crack mouth sliding displacement plots have been obtained in closed form. Proper normalization of the solution shows that the structural response is affected only by four dimensionless parameters. According to the parameter values, the load-displacement curves can exhibit a maximum or not. In the first case, we have derived also an equation providing the process zone size at the maximum load and hence the load itself, thus generalizing to plated beams a previous result valid for direct shear tests (Yuan et al., 2004). It has been emphasized that the present cohesive zone model reverts to the Linear Elastic Fracture Mechanics-Equivalent Beam model for an infinitely stiff and perfectly brittle interface. We further showed that simple Linear Elastic Fracture Mechanics-Equivalent Beam predictions of the failure load are un-conservative, thus justifying the need for the proposed Cohesive Crack Model approach. On the other hand, we showed that the maximum loads predicted by the Cohesive Crack Model are

in good agreement with the estimates provided by the Finite Fracture Mechanics criterion, the latter one being much easier to implement.

The last part of the paper presented a parametric analysis highlighting the effects of material properties and geometry dimensions on debonding load, elastic stiffness and global structural response. In particular, we analyzed the effect of the reinforcement stiffness, of the interfacial cohesive law, of the relative reinforcement length and of the structural size (i.e. the so-called size effect). While a direct comparison with experimental results needs to take into account the basic assumptions used to derive the model (for instance, the interaction of interfacial debonding with flexural/shear cracks in the case of a concrete beam has not been considered), the authors believe that the present parametric investigation can be exploited within the development of design methods for beam strengthening.

Acknowledgements

Laura De Lorenzis would like to acknowledge the European Research Council, ERC Starting Researcher Grant "INTERFACES - Mechanical modeling of interfaces in advanced materials and structures", Grant Agreement N. 279439.

References

Bennati S., Dardano N., Valvo P.S. (2012) A mechanical model for FRP-strengthened beams in bending. Frattura ed Integrità Strutturale 22:39-55.

Büyüközturk O., Leung C., Hearing B., Gunes O. (1998) Delamination criterion for concrete beams retrofitted with FRP laminates. In: Fracture Mechanics of Concrete Structures, Proceedings of FraMCoS-3. 1771-1782. Eds: Mihashi H., Rokugo K. AEDIFICATIO, Freiburg, Germany.

Caggiano A., Martinelli E., Faella C. (2012) A fully-analytical approach for modelling the response of FRP plates bonded to a brittle substrate. International Journal of Solids and Structures 49:2291-300.

Campi F., Monetto I. (2013) Analytical solutions of two-layer beams with interlayer slip and bi-linear interface law. International Journal of Solids and Structures 50:687-98

Carloni C., Subramaniam K.V. (2010) Direct determination of cohesive stress transfer during debonding of FRP from concrete. Composite Structures 93:184-92.

Carpinteri A. (1982) Notch sensitivity in fracture testing of aggregative materials. Engineering Fracture Mechanics 16:467-81.

Carpinteri A. (1989) Cusp catastrophe interpretation of fracture instability. Journal of the Mechanics and Physics of Solids. 37:567-82.

Carpinteri A., Cornetti P. (2011) Modelling the FRP-concrete delamination by means of an exponential softening law. Engineering Structures 33:1988-2001.

Carpinteri A., Cornetti P., Lacidogna G., Paggi M. (2009a). Towards a unified approach for the analysis of failure modes in FRP-retrofitted concrete beams. Advances in Structural Engineering 12:715-29.

Carpinteri A., Cornetti P., Pugno N. (2009b) Edge debonding in FRP strengthened beams: Stress versus energy failure criteria. Engineering Structures 31:2436-47.

Carpinteri A., Paggi M. (2010) Analysis of snap-back instability due to end-plate debonding in strengthened beams. Journal of Engineering Mechanics-ASCE 136:199-208.

Colombi P. (2006) Reinforcement delamination of metallic beams strengthened by FRP strips: Fracture mechanics based approach. Engineering Fracture Mechanics 73:1980-95.

Cornetti P., Pugno N., Carpinteri A., Taylor D. (2006) Finite fracture mechanics: A coupled stress and energy failure criterion. Engineering Fracture Mechanics 73: 2021-33.

Cornetti P., Mantič V., Carpinteri A. (2012) Finite Fracture Mechanics at elastic interfaces. International Journal of Solids and Structures 49:1022-32.

Cottone A., Giambanco G. (2009) Minimum bond length and size effects in FRP-substrate bonded joints. Engineering Fracture Mechanics 76:1957-76.

De Lorenzis L. (2012) Some recent results and open issues on interface modeling in civil engineering structures. Materials and Structures 45:477-503.

De Lorenzis L., Fernando D., Teng J-G. (2013) Coupled mixed-mode cohesive zone modeling of interfacial debonding in simply supported plated beams. International Journal of Solids and Structures 50:2477-94.

De Lorenzis L., Zavarise G. (2009) Cohesive zone modeling of interfacial stresses in plated beams. International Journal of Solids and Structures 46:4181-91.

Dehghani E., Daneshjoo F., Aghakouchak A.A., Khaji N. (2012) A new bond-slip model for adhesive in CFRP-steel composite systems. Engineering Structures 34:447-54.

Ferracuti B., Savoia M., Mazzotti C. (2006) A numerical model for FRP-concrete delamination. Composites Part B: Engineering 37:356-64.

Ferracuti B, Savoia M, Mazzotti C. (2007) Interface law for FRP-concrete delamination. Composite Structures 80:523-31.

Foraboschi P. (2009) Analytical Solution of Two-Layer Beam Taking into Account Nonlinear Interlayer Slip. Journal of Engineering Mechanics-ASCE 135:1129-46.

Greco F., Lonetti P., Nevone Blasi P. (2007) An analytical investigation of debonding problems in beams strengthened using composite plates. Engineering Fracture Mechanics 74:346-72.

Henninger C., Leguillon D., Martin E. (2007) Crack initiation at a V-notch – comparison between a brittle fracture criterion and the Dugdale cohesive model. Comptes Rendu Mécanique 335:388-393.

Leung C.K.Y., Tung W.K. (2006) Three-parameter model for debonding of FRP plate from concrete substrate. Journal of Engineering Mechanics-ASCE 132:509-18.

Lu X.Z., Teng J-G., Ye L.P., Jiang J.J. (2005) Bond-slip models for FRP sheets/plates bonded to concrete. Engineering Structures 27:920–37.

Mantič, V. (2009) Interface crack onset at a circular cylindrical inclusion under a remote transverse tension. Application of a coupled stress and energy criterion. International Journal of Solids and Structures 46:1287–1304.

Pellegrino C., D'Antino T. (2013) Experimental behaviour of existing precast prestressed reinforced concrete elements strengthened with cementitious composites. Composites Part B: Engineering 55:31-40

Rabinovitch O. (2004) Fracture-mechanics failure criteria for RC beams strengthened with FRP strips - a simplified approach. Composite Structures 64:479-92.

Rabinovitch O. (2008a) Cohesive interface modeling of debonding failure in FRP strengthened beams. Journal of Engineering Mechanics-ASCE 134:578-588.

Rabinovitch O. (2008b) Debonding analysis of fiber-reinforced-polymer strengthened beams: cohesive zone modeling versus a linear elastic fracture mechanics approach. Engineering Fracture Mechanics 75:2842-59.

Távara L., Mantič V., Graciani E., París F. (2011) BEM analysis of crack onset and propagation along fiber-matrix interface under transverse tension using a linear elastic-brittle interface model. Engineering Analysis with Boundary Elements 35:207-222.

Smith S., Teng J. (2001) Interfacial stresses in plated beams. Engineering Structures 23: 857-71.
Taljsten B. (1997) Strengthening of beams by plate bonding. Journal of Materials in Civil Engineering-ASCE 9:206-12.

Wang S., Harvey C.M., Guan L. (2013) Partition of mixed modes in layered isotropic double cantilever beams with non-rigid cohesive interfaces. Engineering Fracture Mechanics 111:1-25.

Yuan H., Teng J.G., Seracino R., Wu Z.S., Yao J. (2004) Full-range behavior of FRP-to-concrete bonded joints. Engineering Structures 26: 553-65.

Appendix A

By means of the axial equilibrium of the reinforcement (eqn(11c)), the stress in the FRP plate is readily achieved as:

$$\sigma_{\mathrm{r}}(z)=\frac{N_{\mathrm{r}}(z)}{t_{\mathrm{r}}h_{\mathrm{r}}}=\frac{1}{h_{\mathrm{r}}}\int_{z}^{z_{\mathrm{r}}}\tau(z')\,\mathrm{d}z' \tag{A1}$$

that is, in dimensionless form:

$$\frac{\sigma_{\mathrm{r}}}{\tau_{\mathrm{p}}l_{\mathrm{ch}}/h_{\mathrm{r}}}(\zeta)=\int_{\zeta}^{\zeta_{\mathrm{r}}}\frac{\tau}{\tau_{\mathrm{p}}}(\zeta')\,\mathrm{d}\zeta' \tag{A2}$$

During the elastic stage, the stress in the reinforcement is achieved upon substitution of eqn (24) into eqn (A2):

$$\frac{\sigma_{\mathrm{r}}}{\tau_{\mathrm{p}}l_{\mathrm{ch}}/h_{\mathrm{r}}}(\zeta)=\Pi\left[(\zeta_{\mathrm{r}}-\zeta)+\frac{\alpha\,(\cosh\zeta_{\mathrm{r}}-\cosh\zeta)-\sinh(\zeta_{\mathrm{r}}-\zeta)}{\cosh\zeta_{\mathrm{r}}}\right] \tag{A3}$$

For what concerns the second and third stages, the stress in the reinforcement is obtained by substitution of eqns (28) and (32) into eqn (A2). In the process zone it is equal to:

$$\begin{aligned}\frac{\sigma_{\mathrm{r}}}{\tau_{\mathrm{p}}l_{\mathrm{ch}}/h_{\mathrm{r}}}(\zeta)=&(1-\Pi)\left(\frac{\tan[\mu_2(\zeta_{\mathrm{r}}-\overline{\zeta})]}{\mu_2}+\frac{\cosh\overline{\zeta}-\cosh\zeta}{\sinh\overline{\zeta}}\right)+\\&+\Pi\left(\lambda-\zeta-\frac{\alpha}{\cos[\mu_2(\zeta_{\mathrm{r}}-\overline{\zeta})]}+\frac{1-\cosh(\overline{\zeta}-\zeta)}{\sinh\overline{\zeta}}\right),\ \overline{\zeta}\le\zeta\le\zeta_{\mathrm{r}}\end{aligned} \tag{A4}$$

whereas its expression in the elastic region is:

$$\frac{\sigma_{\mathrm{r}}}{\tau_{\mathrm{p}}l_{\mathrm{ch}}/h_{\mathrm{r}}}(\zeta)=\frac{(1-\Pi)\,\sin\mu_2(\zeta_{\mathrm{r}}-\zeta)+\mu_2\,\Pi\left[(\lambda-\zeta)\cos\mu_2(\zeta_{\mathrm{r}}-\overline{\zeta})-\alpha\cos\mu_2(\zeta-\overline{\zeta})\right]}{\mu_2\cos\mu_2(\zeta_{\mathrm{r}}-\overline{\zeta})},\ 0\le\zeta\le\overline{\zeta} \tag{A5}$$

Appendix B

To evaluate the mid-span deflection during the elastic stage, one simply has to insert eqn (24) and (25) into eqn (42). This leads to:

$$\frac{v}{v_{Jou}} = \Pi \frac{\left[(1+\rho)\lambda^3 + 3\rho\alpha^3\right] + 9\rho\left[\lambda + \alpha - 2\alpha \operatorname{sech}\zeta_r + (\alpha^2 - 1)\tanh\zeta_r\right]}{(1+4\rho)\lambda^3} \tag{B1}$$

For what concerns the mid-span deflection during the second and third stages, the integral in eqn(42) has to be split in two pieces, one for elastic region, one for the process zone:

$$\int_0^{\zeta_r} \delta(\zeta)\, d\zeta = \int_0^{\overline{\zeta}} \delta(\zeta)\, d\zeta + \int_{\overline{\zeta}}^{\zeta_r} \delta(\zeta)\, d\zeta \tag{B2}$$

By means of eqn (28), the former term reads:

$$\int_0^{\overline{\zeta}} \delta(\zeta)\, d\zeta = \frac{1-2\Pi}{\sinh\overline{\zeta}}(\cosh\overline{\zeta} - 1) + \Pi\overline{\zeta} \tag{B3}$$

While, by eqn (30), the latter one is:

$$\int_{\overline{\zeta}}^{\zeta_r} \delta(\zeta)\, d\zeta = \mu(\zeta_r - \overline{\zeta}) + (\mu - 1)\left\{\frac{\Pi - 1}{\mu_2}\tan\mu_2(\zeta_r - \overline{\zeta}) - \Pi\left[(\lambda - \overline{\zeta}) - \alpha\sec\mu_2(\zeta_r - \overline{\zeta})\right]\right\} \tag{B4}$$

Substitution of eqns (B3-B4) into eqn (42) provides the desired value of the deflection during the debonding process.

Appendix C

In this appendix we provide the explicit expression for the integrals appearing in the formulation of the FFM criterion. For what concerns the integral in eqn (54), we have:

$$\int_{\zeta_r-\xi}^{\zeta_r}\left[1+\frac{\alpha\sinh\zeta-\cosh(\zeta_r-\zeta)}{\cosh\zeta_r}\right]\mathrm{d}\zeta=\xi+\alpha-\frac{\alpha\cosh(\zeta_r-\xi)+\sinh\xi}{\cosh\zeta_r} \tag{C1}$$

while the integral in eqn (56) yields:

$$\int_{\zeta_r-\xi}^{\zeta_r}\left[1+(\lambda-\zeta_r')\tanh\zeta_r'-\mathrm{sech}\zeta_r'\right]^2\,\mathrm{d}\zeta_r'=$$

$$=\xi\left(1+\alpha^2+\alpha\xi+\frac{\xi^3}{3}\right)-2\left[(\alpha+\xi)\,\mathrm{sech}(\zeta_r-\xi)-\alpha\,\mathrm{sech}\,\zeta_r\right]+\left[(\alpha+\xi)^2-1\right]\tanh(\zeta_r-\xi)-(\alpha^2-1)\tanh\zeta_r \tag{C2}$$

Appendix D

Let us consider an unreinforced TPB beam subjected to a constant shear stress τ_p at the soffit directed toward the mid-span acting on the region $-z_r < z < +z_r$. Elementary beam theory allows one to compute the mid-span deflection as:

$$v = \frac{P(2l)^3}{48E_b I_b} - \frac{\tau_p t_r h_b z_r^2 (2l + a)}{12E_b I_b} \tag{D1}$$

which, in dimensionless form, reads:

$$\frac{v}{v_{Jou}} = \Pi - \frac{3\rho\zeta_r^2 (3\lambda - \zeta_r)}{2(1+4\rho)\lambda^3} \tag{D2}$$

Equation (D2) is the equation of the asymptote to the elastic-perfectly plastic interface case considered in fig. 14.

Figure captions

Figure 1. Plated beam in a three-point-bending configuration (a). Cross section (b).

Figure 2. Symmetry is exploited to study only the right half of the beam (a). Cross section (b) and detail of the reference system.

Figure 3. Dimensionless load vs. displacement curve according to LEFM ($\rho = 0.4$, $z_r/l = 0.7$).

Figure 4. Differential element of the plated beam.

Figure 5. Interfacial cohesive law with linear softening.

Figure 6. Shear stress along the interface at the end of the elastic stage in the right half of the beam for $\lambda = 20$ and $\zeta_r = 16$. The origin corresponds to the mid-span and the right extreme to the FRP edge. The dashed line represents the shear stress according to Jourawsky's formula (eqn(5)).

Figure 7. Shear stress along the interface during the debonding process for $\lambda = 20$, $\zeta_r = 16$ and $\mu = 5$. From right to left, curves refer to: the end of the elastic stage, the attainment of the maximum load (dashed line), the beginning of the detachment, and a detached length equal to 25%, 50% and 75% of the initial bonded length.

Figure 8. Normal stress in the reinforcement during the debonding process for $\lambda = 20$, $\zeta_r = 16$ and $\mu = 5$. From right to left, curves refer to: the end of the elastic stage; the attainment of the maximum load (dashed line), the beginning of the detachment, and a detached length equal to 25%, 50% and 75% of the initial reinforced length.

Figure 9. Load vs. mid-span deflection (dimensionless plot) for $\lambda = 10$, $\zeta_r = 7$, $\mu = 5$ and $\rho = 0.4$. The green line represents the elastic stage (from the origin up to point A); the blue curve the elastic-softening stage (from point A to point B); the red curve the elastic-softening-debonding stage (after point B). Small black dots in the last stage correspond to equispaced positions of the real crack tip. The black thin line corresponds to LEFM predictions and the dashed line to the linear elastic unreinforced beam.

Figure 10. Load vs. mid-span deflection (dimensionless plots) for different values of the parameters λ, μ and ζ_r (ρ is fixed and equal to 0.4): the structural behaviour may show both snap-back and snap-through instabilities (a); only snap-through instability (b); none (c).

Figure 11. Structural instability map for relative reinforcement length z_r/l equal to 0.8. The right curve is slightly affected also by the mechanical percentage of reinforcement ρ, herein taken equal to 0.125.

Figure 12. Load vs. CMSD (dimensionless plots) according to different values of the parameters λ, μ and ζ_r (a,b,c). The CMSD is always monotonically increasing, whereas the mid-span deflection is not (d). Note that in order to compare the CMSD and the mid-span deflection, both ρ and the beam slenderness have to be specified (here $\rho = 0.4$ and $2l / h_b = 4$).

Figure 13. Normalized debonding load vs. interface ductility μ according to the LEFM-EB, FFM, CCM and approximate CCM (eqn (47)) models. The relative reinforcement length z_r / l is fixed and equal to 0.8, while the parameter λ is equal to 5 (a), 10 (b) and 15 (c). Beyond certain μ values, both

FFM and CCM do not provide a solution because the load is monotonically increasing and the maximum disappears.

Figure 14. Load vs. mid-span deflection (dimensionless plot): effect of the reinforcement stiffness. The curves are plotted for $n = E_r/E_b$ equal to 4, 6, 8, 10, 12. The thick line is the reference case (n = 8).

Figure 15. Load vs. mid-span deflection (dimensionless plot, (b)): effect of the interface cohesive law (a) for fixed k and τ_p values. The curves are plotted for μ equal to 1 (elastic-perfectly brittle case), 5, 10, 20, 40 and ∞ (elastic-perfectly plastic case). The thick line is the reference case (μ = 10).

Figure 16. Load vs. mid-span deflection (dimensionless plot, (b)): effect of the interface cohesive law (a) for fixed k and $\mathcal{G}_c$ values. The curves are plotted for μ equal to 2, 5, 10, 15, 20. The thick line is the reference case (μ = 10).

Figure 17. Load vs. mid-span deflection (dimensionless plot): size effect. The curves are plotted for brittleness number $s_E = \mathcal{G}_c/(\tau_p\, h_r)$ equal to 0.015, 0.03, 0.06, 0.12, 0.24, corresponding to a size range of 1:16. The thick line is the reference case (s_E = 0.06). Note that s_E is inversely proportional to the structural size.

Figure 18. Load vs. mid-span deflection (dimensionless plot): effect of the relative bond length. The curves are plotted for ratios z_r/l equal to 0.5, 0.6, 0.7, 0.8, 0.9. The thick line is the reference case (z_r/l = 0.8).

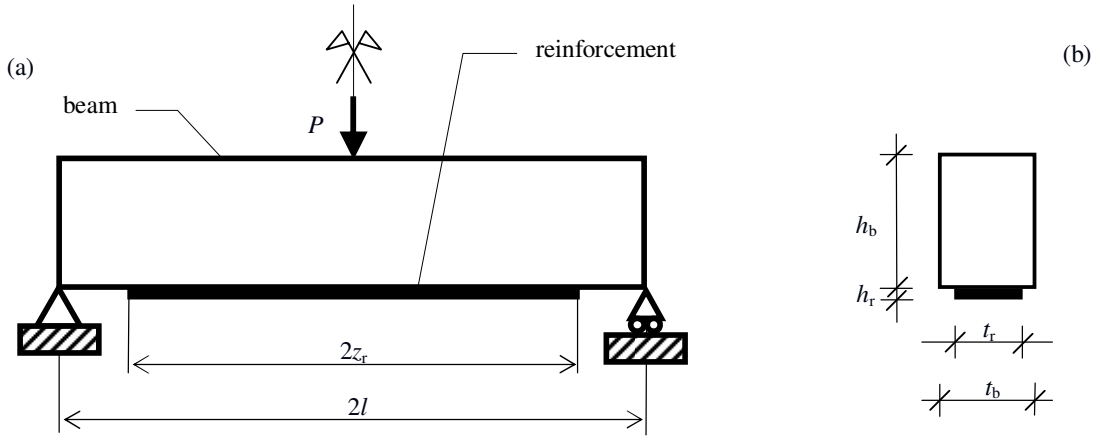

Figure 1. Plated beam in a three-point-bending configuration (a). Cross section (b).

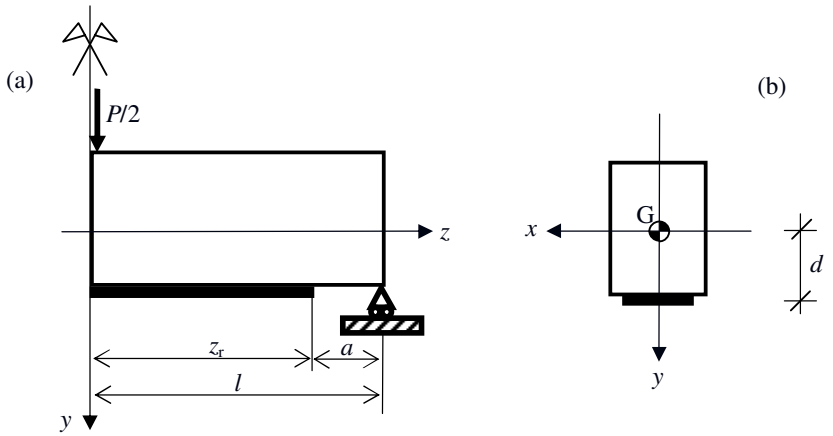

Figure 2. Simmetry is exploited to study only the right half of the beam (a). Cross section (b) and detail of the reference system.

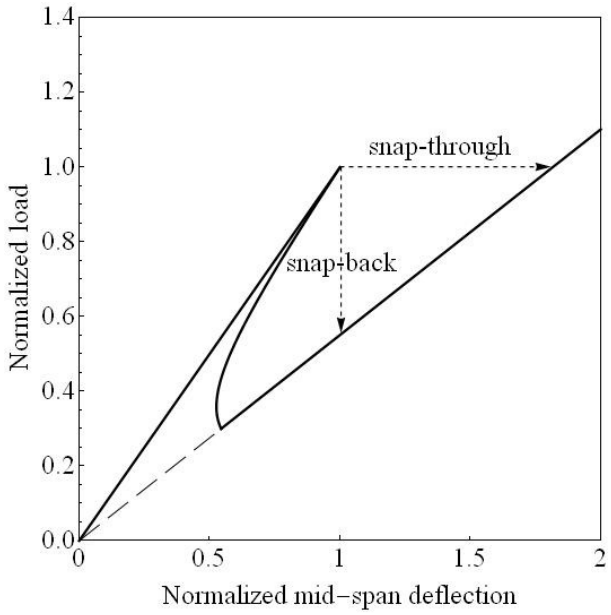

Figure 3. Dimensionless load vs. displacement curve according to LEFM ($\rho = 0.4$, $z_r/l = 0.7$).

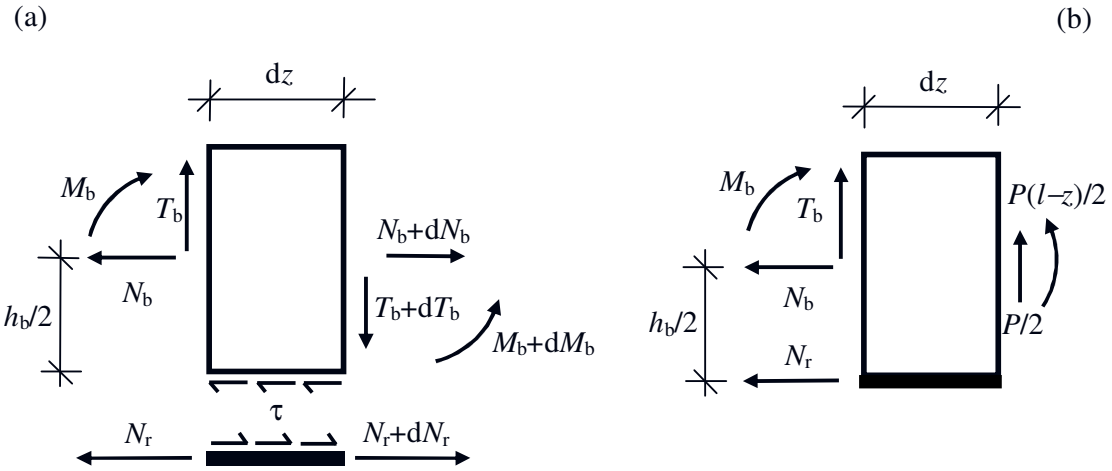

Figure 4. Differential element of the plated beam.

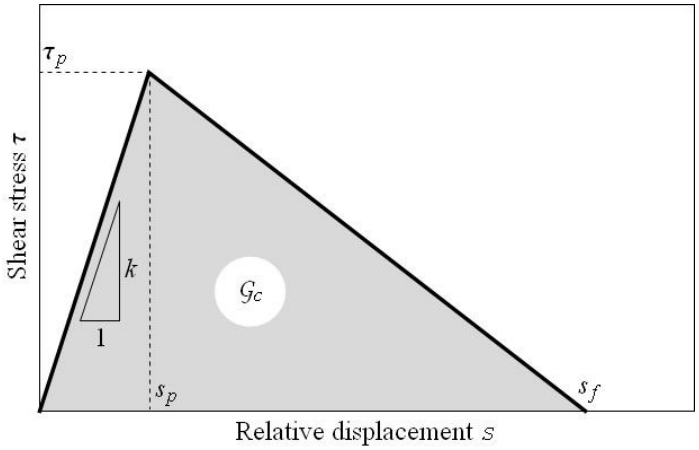

Figure 5. Interfacial cohesive law with linear softening.

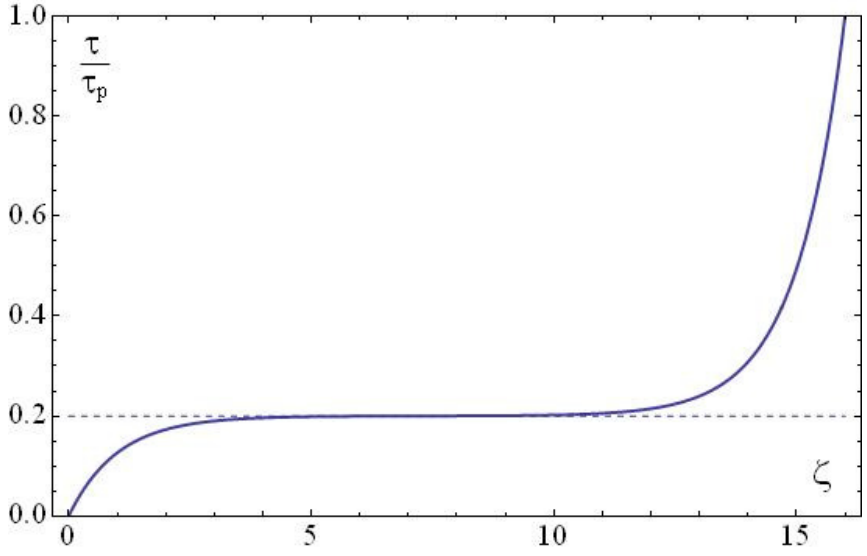

Figure 6. Shear stress along the interface at the end of the elastic stage in the right half of the beam for $\lambda = 20$ and $\zeta_r = 16$. The origin corresponds to the mid-span and the right extreme to the FRP edge. The dashed line represents the shear stress according to Jourawsky's formula (eqn(5)).

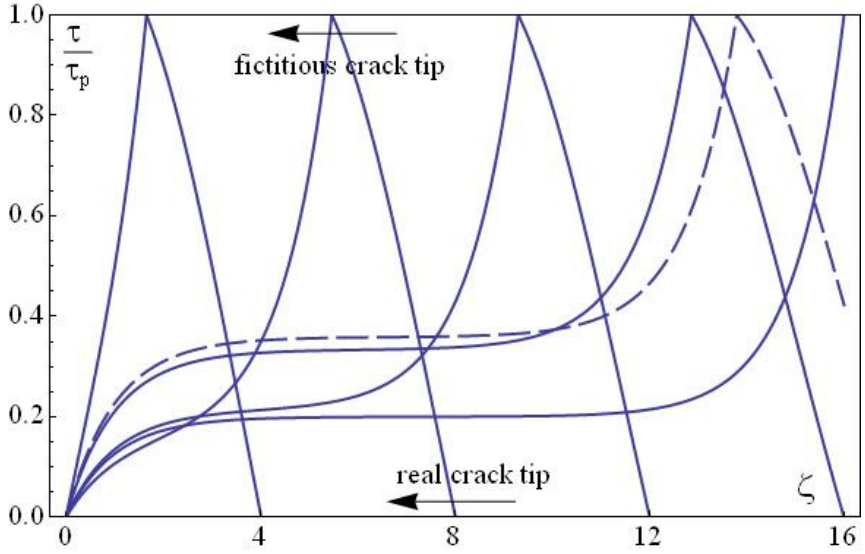

Figure 7. Shear stress along the interface during the debonding process for $\lambda = 20$, $\zeta_r = 16$ and $\mu = 5$. From right to left, curves refer to: the end of the elastic stage, the attainment of the maximum load (dashed line), the beginning of the detachment, and a detached length equal to 25%, 50% and 75% of the initial bonded length.

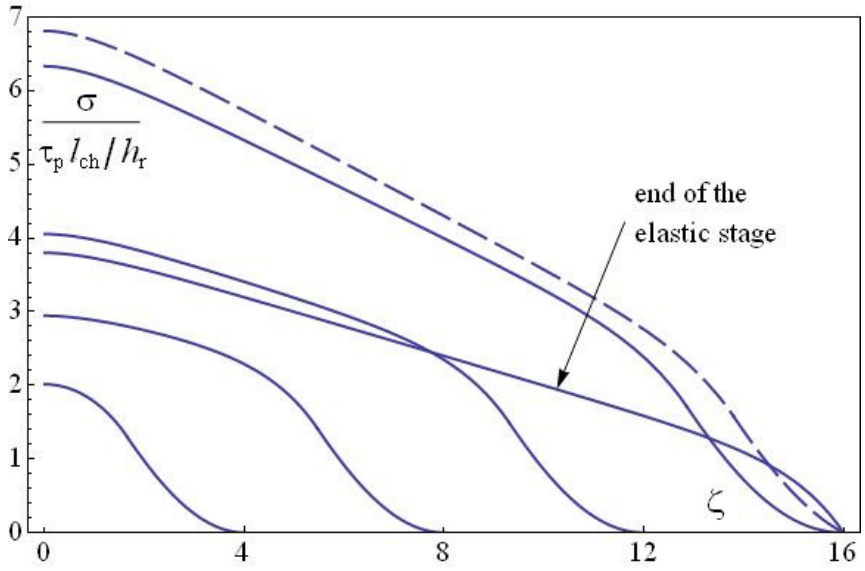

Figure 8. Normal stress in the reinforcement during the debonding process for $\lambda = 20$, $\zeta_r = 16$ and $\mu = 5$. From right to left, curves refer to: the end of the elastic stage; the attainment of the maximum load (dashed line), the beginning of the detachment, and a detached length equal to 25%, 50% and 75% of the initial reinforced length.

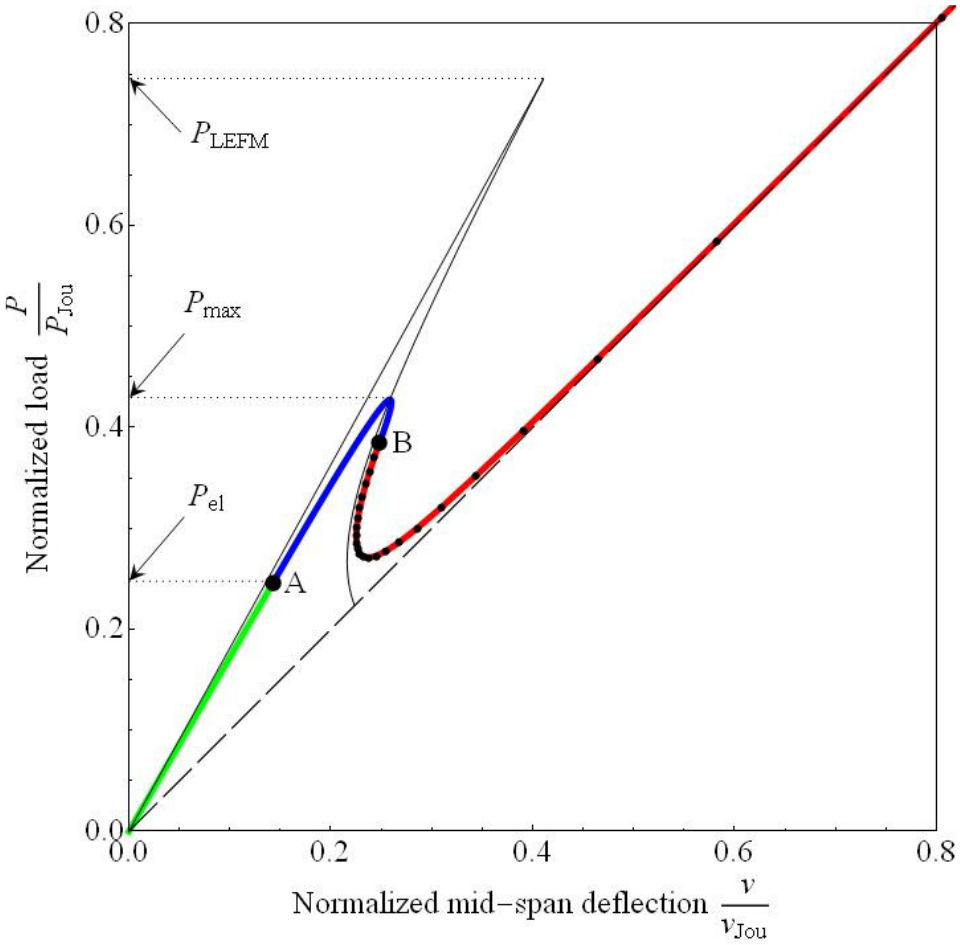

Figure 9. Load vs. mid-span deflection (dimensionless plot). The green line represents the elastic stage (from the origin up to point A); the blue curve the elastic-softening stage (from point A to point B); the red curve the elastic-softening-debonding stage (after point B). Small black dots in the last stage correspond to equispaced positions of the real crack tip. The black thin line corresponds to LEFM predictions and the dashed line to the linear elastic unreinforced beam.

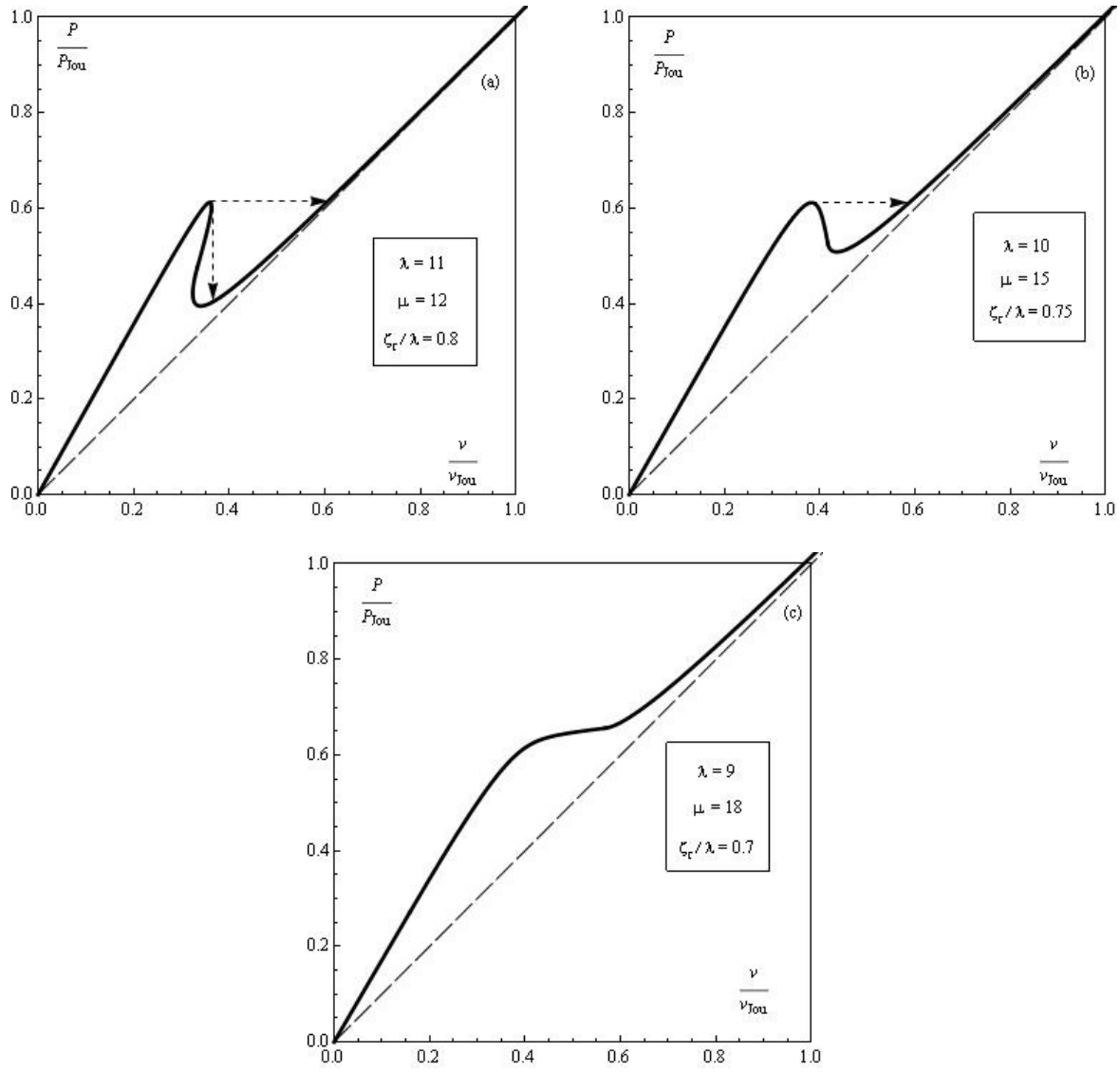

Figure 10. Load vs. mid-span deflection (dimensionless plots) for different values of the parameters λ, μ and ζ_r (ρ is fixed and equal to 0.4): the structural behaviour may show both snap-back and snap-through instabilities (a); only snap-through instability (b); none (c).

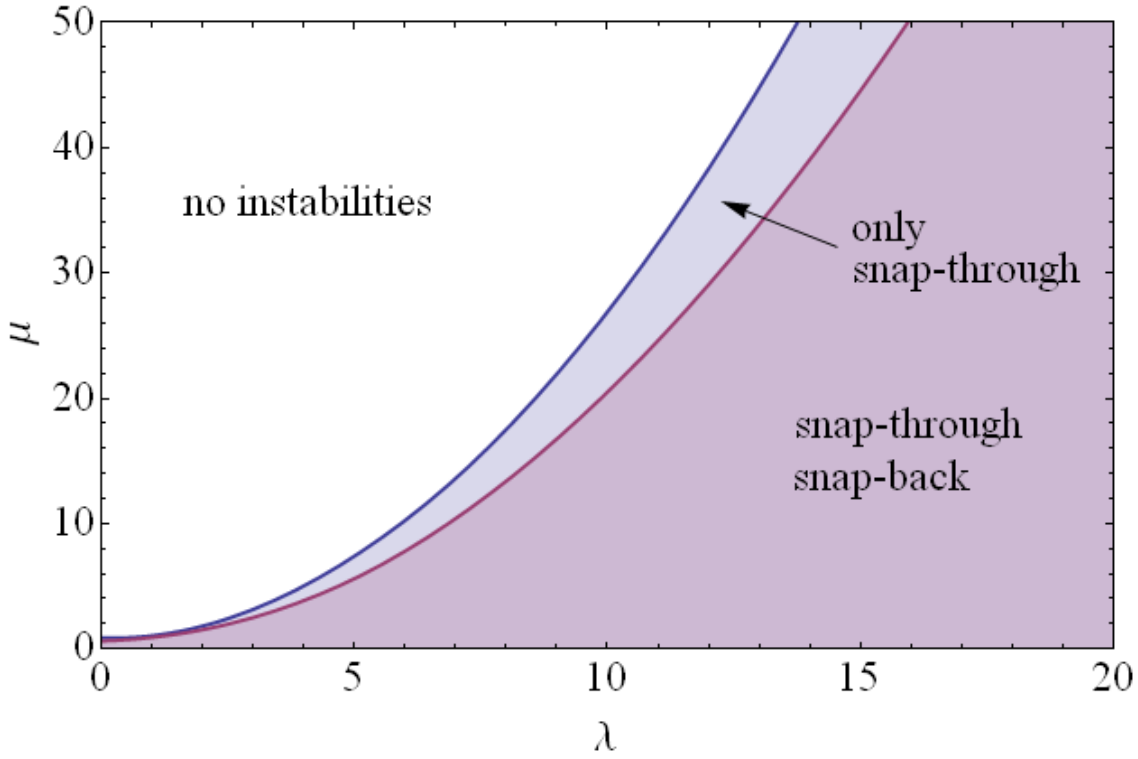

Figure 11. Structural instability map for relative reinforcement length z_r/l equal to 0.8. The right curve is slightly affected also by the mechanical percentage of reinforcement ρ, herein taken equal to 0.125.

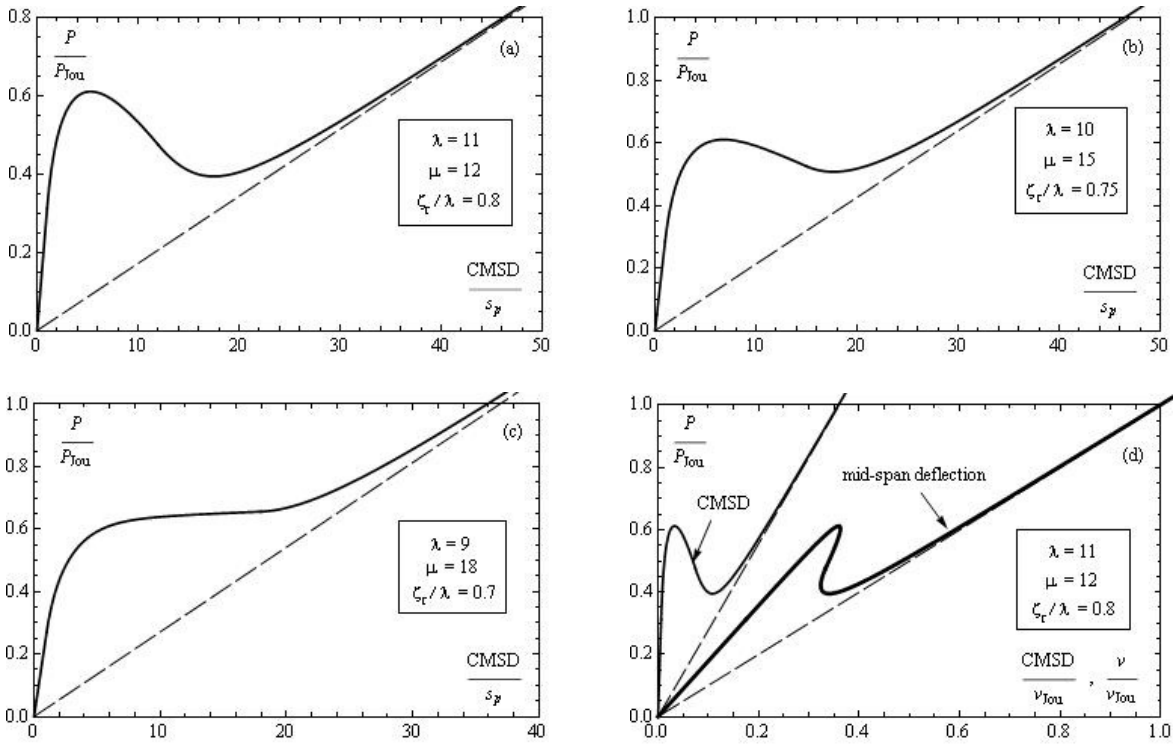

Figure 12. Load vs. CMSD (dimensionless plots) according to different values of the parameters λ, μ and ζ_r (a,b,c). The CMSD is always monotonically increasing, whereas the mid-span deflection is not (d). Note that in order to compare the CMSD and the mid-span deflection, both ρ and the beam slenderness have to be specified (here ρ = 0.4 and $2l / h_b = 4$).

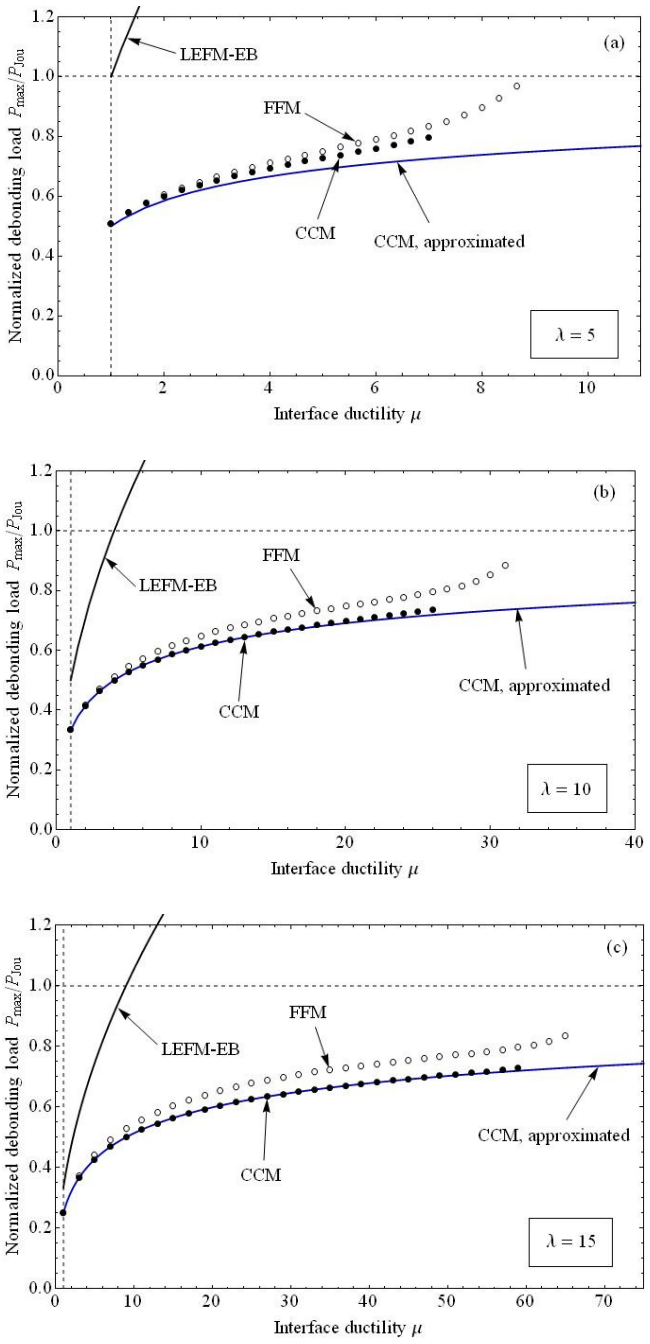

Figure 13. Normalized debonding load vs. interface ductility μ according to the LEFM-EB, FFM, CCM and approximate CCM (eqn (47)) models. The relative reinforcement length z_r / l is fixed and equal to 0.8, while the parameter λ is equal to 5 (a), 10 (b) and 15 (c). Beyond certain μ values, both FFM and CCM do not provide a solution because the load is monotonically increasing and the maximum disappears.

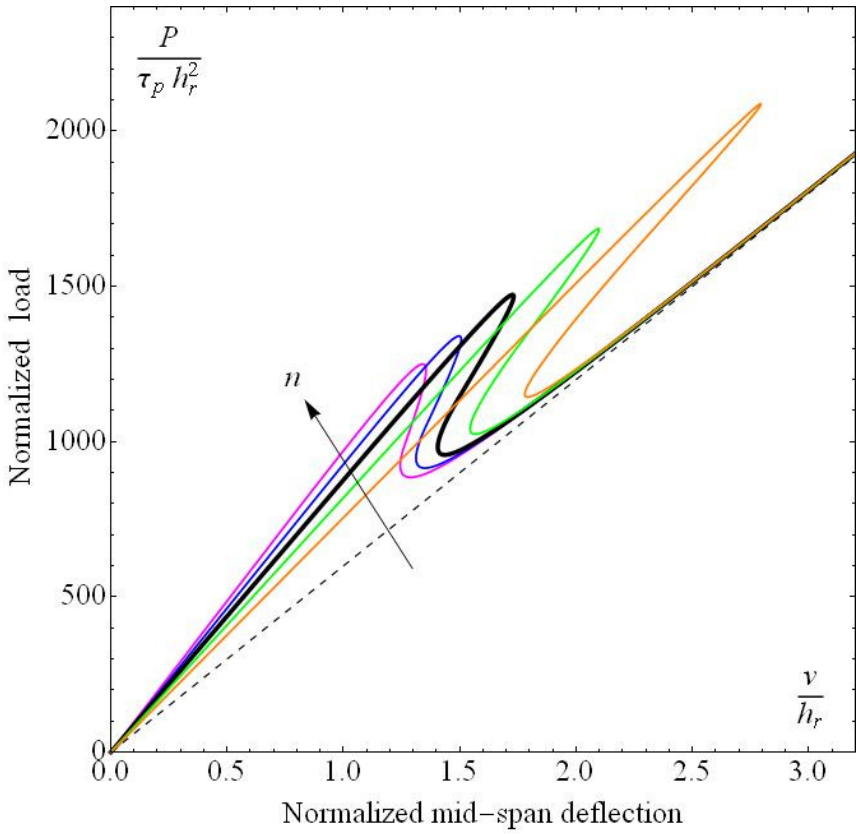

Figure 14. Load vs. mid-span deflection (dimensionless plot): effect of the reinforcement stiffness. The curves are plotted for $n = E_r/E_b$ equal to 4, 6, 8, 10, 12. The thick line is the reference case (n = 8).

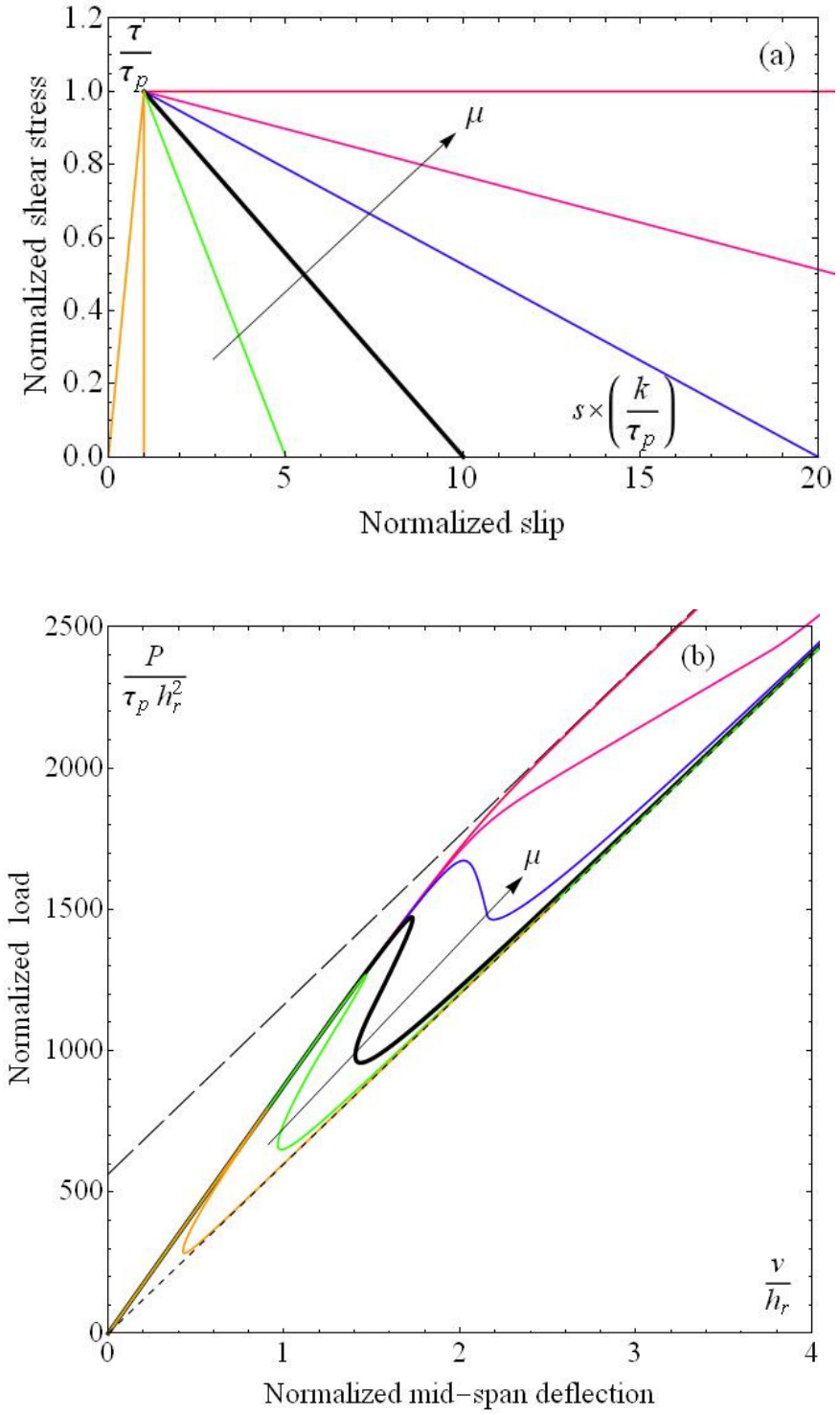

Figure 15. Load vs. mid-span deflection (dimensionless plot, (b)): effect of the interface cohesive law (a) for fixed k and τ_p values. The curves are plotted for μ equal to 1 (elastic-perfectly brittle case), 5, 10, 20, 40 and ∞ (elastic-perfectly plastic case). The thick line is the reference case (μ = 10).

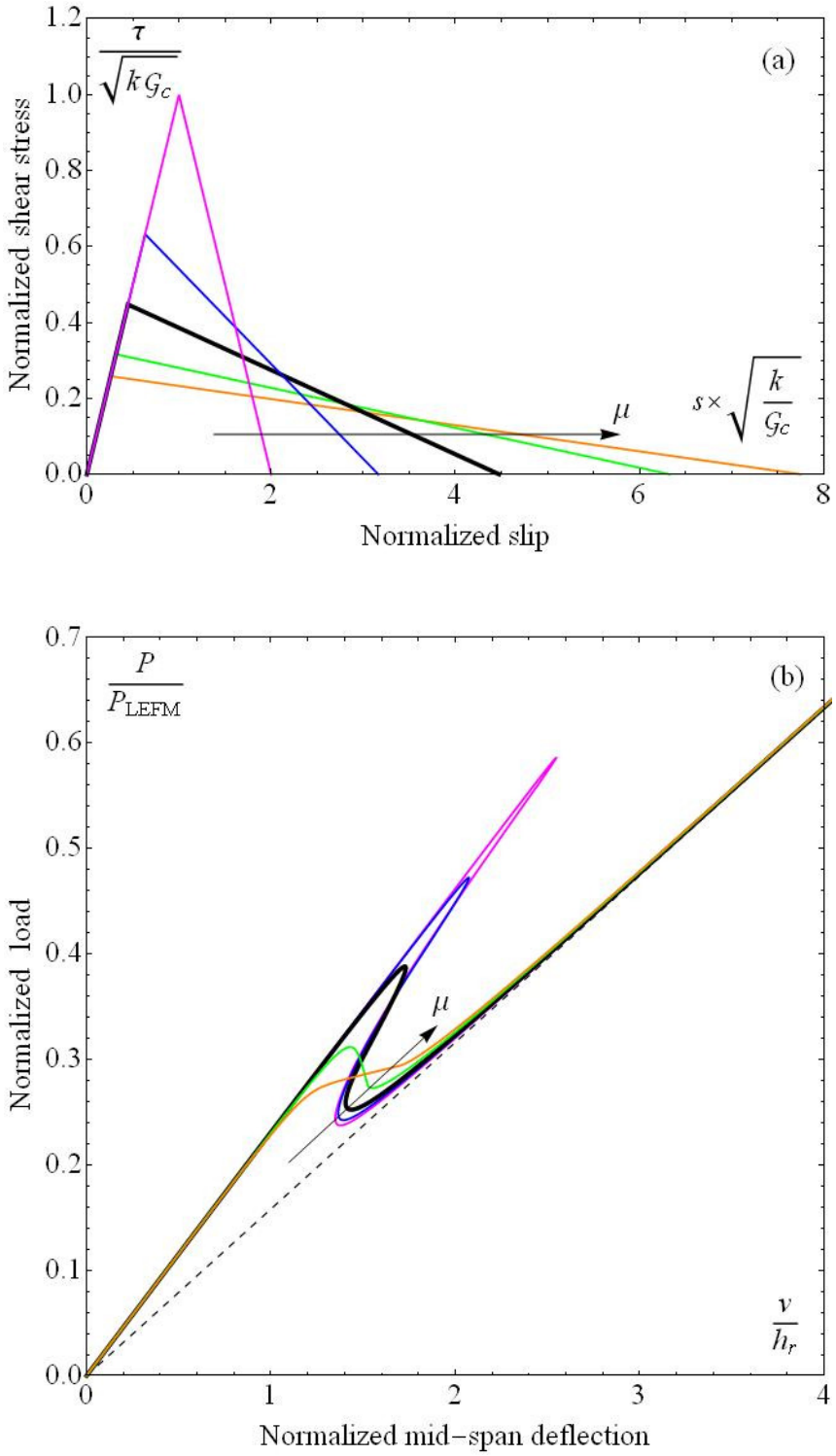

Figure 16. Load vs. mid-span deflection (dimensionless plot, (b)): effect of the interface cohesive law (a) for fixed k and $\mathcal{G}_c$ values. The curves are plotted for μ equal to 2, 5, 10, 15, 20. The thick line is the reference case (μ = 10).

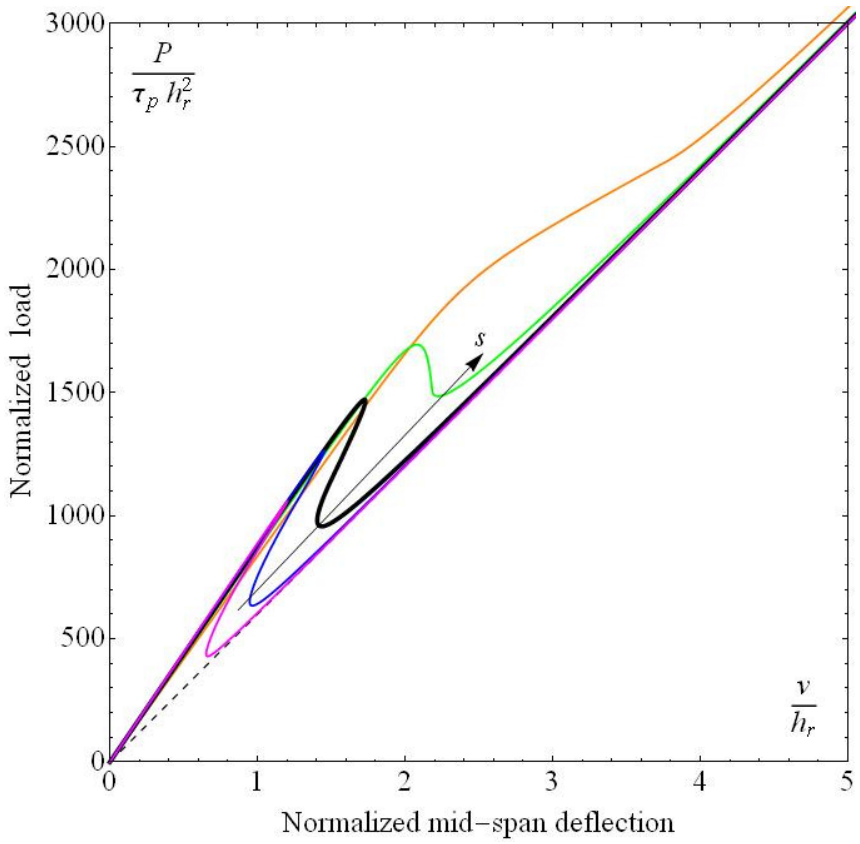

Figure 17. Load vs. mid-span deflection (dimensionless plot): size effect. The curves are plotted for brittleness number $s_E = \mathcal{G}_c/(\tau_p\, h_r)$ equal to 0.015, 0.03, 0.06, 0.12, 0.24, corresponding to a size range of 1:16. The thick line is the reference case ($s_E = 0.06$). Note that s is inversely proportional to the structural size.

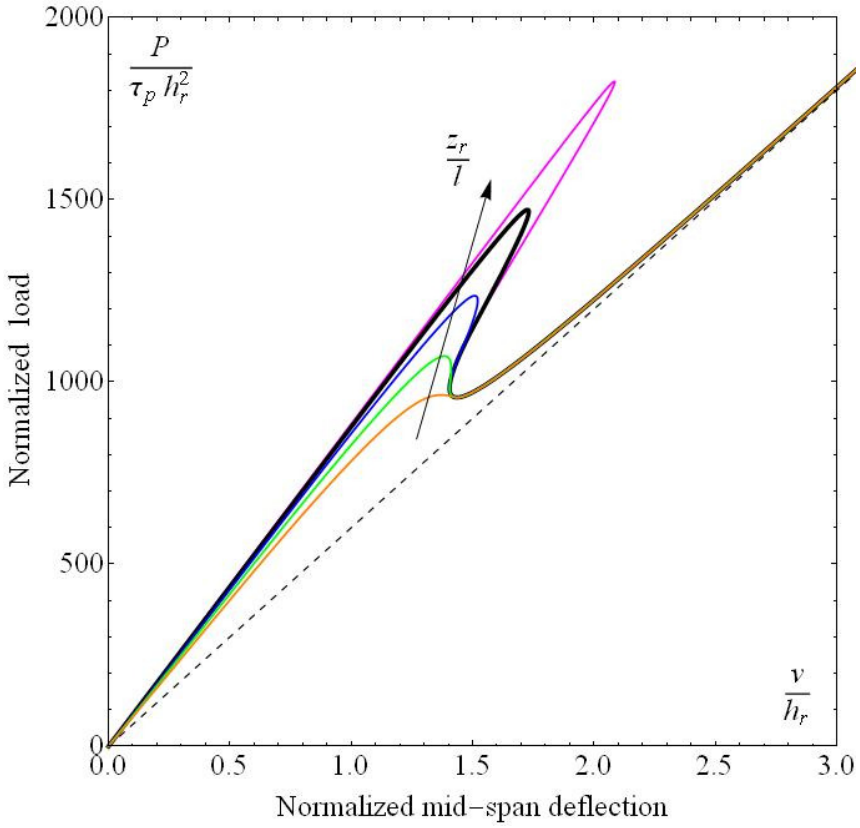

Figure 18. Load vs. mid-span deflection (dimensionless plot): effect of the relative bond length. The curves are plotted for ratios z_r/l equal to 0.5, 0.6, 0.7, 0.8, 0.9. The thick line is the reference case ($z_r/l = 0.8$).